Integrated pseudotime analysis of human pre-implantation embryo single-cell transcriptomes reveals the dynamics of lineage specification

Graphical abstract
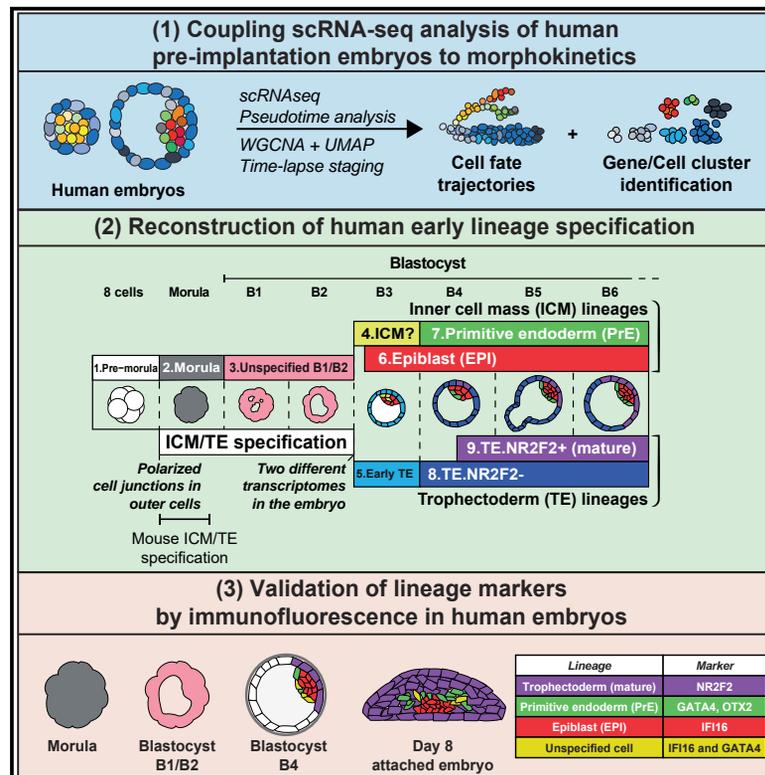
Authors

Dimitri Meistermann,
Alexandre Bruneau,
Sophie Loubersac, ...,
Jérémie Bourdon, Thomas Fréour,
Laurent David

Correspondence

thomas.freour@chu-nantes.fr (T.F.),
laurent.david@univ-nantes.fr (L.D.)

In brief

Meistermann et al. use scRNA-seq, pseudotime analysis, and immunofluorescence validation to reconstruct the sequence of molecular events occurring in time-lapse-staged human preimplantation embryos. Their findings clarify specification, timing, and cell transcriptomes across early stages of human development.

Highlights

- Distinct trophectoderm/epiblast signatures arise at the B2–B3 blastocyst stages

- IFI16 is broadly expressed in the ICM and then restricted to epiblast after implantation

- NR2F2 arises from the polar TE in late blastocysts and then spreads to all TE cells

- Transcriptomics analysis suggests that PrE emerges from EPI in late blastocysts

CellPress

Resource

Integrated pseudotime analysis of human pre-implantation embryo single-cell transcriptomes reveals the dynamics of lineage specification

Dimitri Meistermann,[1,3,13] Alexandre Bruneau,[1,13] Sophie Loubersac,[1,2,13] Arnaud Reignier,[1,2] Julie Firmin,[1,2] Valentin François-Campion,[1] Stéphanie Kilens,[1] Yohann Lelièvre,[3] Jenna Lammers,[2] Magalie Feyeux,[1,4] Phillipe Hulin,[4] Steven Nedellec,[4] Betty Bretin,[1] Gaël Castel,[1] Nicolas Allègre,[9] Simon Covin,[1] Audrey Bihouée,[4,5] Magali Soumillon,[6,7,8,11] Tarjei Mikkelsen,[6,7,8,12] Paul Barrière,[1,2] Claire Chazaud,[9] Joel Chappell,[10] Vincent Pasque,[10] Jérémie Bourdon,[3] Thomas Fréour,[1,2,*] and Laurent David[1,4,14,*]

[1]Université de Nantes, CHU Nantes, INSERM, Centre de Recherche en Transplantation et Immunologie, UMR 1064, ITUN, 44000 Nantes, France
[2]CHU Nantes, Université de Nantes, Service de Biologie de la Reproduction, 44000 Nantes, France
[3]LS2N, UNIV Nantes, CNRS, Nantes, France
[4]Université de Nantes, CHU Nantes, INSERM, CNRS, SFR Santé, FED 4203, INSERM UMS 016, CNRS UMS 3556, Nantes, France
[5]Institut du Thorax, UNIV Nantes, INSERM, CNRS, Nantes, France
[6]Department of Stem Cell and Regenerative Biology, Harvard University, Cambridge, MA 02138, USA
[7]Broad Institute, Cambridge, MA 02142, USA
[8]Harvard Stem Cell Institute, Harvard University, Cambridge, MA 02138, USA
[9]GReD Laboratory, Université Clermont Auvergne, CNRS, INSERM, Faculté de Médecine, CRBC, 63000 Clermont-Ferrand, France
[10]KU Leuven – University of Leuven, Department of Development and Regeneration, Institute for Single Cell Omics, Leuven Stem Cell Institute, Herestraat 49, 3000 Leuven, Belgium
[11]Present address: Flexomics LLC, 38 Wareham Street, Fl 3, Boston, MA 02118, USA
[12]Present address: 10x Genomics, 7068 Koll Center Pkwy #401, Pleasanton, CA 94566, USA
[13]These authors contributed equally
[14]Lead contact
*Correspondence: thomas.freour@chu-nantes.fr (T.F.), laurent.david@univ-nantes.fr (L.D.)
https://doi.org/10.1016/j.stem.2021.04.027

SUMMARY

Understanding lineage specification during human pre-implantation development is a gateway to improving assisted reproductive technologies and stem cell research. Here we employ pseudotime analysis of single-cell RNA sequencing (scRNA-seq) data to reconstruct early mouse and human embryo development. Using time-lapse imaging of annotated embryos, we provide an integrated, ordered, and continuous analysis of transcriptomics changes throughout human development. We reveal that human trophectoderm/inner cell mass transcriptomes diverge at the transition from the B2 to the B3 blastocyst stage, just before blastocyst expansion. We explore the dynamics of the fate markers IFI16 and GATA4 and show that they gradually become mutually exclusive upon establishment of epiblast and primitive endoderm fates, respectively. We also provide evidence that NR2F2 marks trophectoderm maturation, initiating from the polar side, and subsequently spreads to all cells after implantation. Our study pinpoints the precise timing of lineage specification events in the human embryo and identifies transcriptomics hallmarks and cell fate markers.

INTRODUCTION

A key question in biology is how cell fate specification takes place in the early human embryo. The main information we have from this period of development is the changes in morphology of the embryo. Concomitant with morphological changes and growth of the embryo, pluripotent epiblast and trophectoderm cells are established. Because human pluripotency is established during human preimplantation development, a better understanding of early human embryogenesis has a strong effect on research in the field of pluripotent stem cells.

Human preimplantation development is also important for fertility treatment and *in vitro* fertilization (IVF) in particular.

The main morphological events during pre-implantation development are compaction and cavitation. Compaction is characterized by the tight interactions that form between cells after the 8-cell stage. Cavitation is formation of a single cavity within the embryo through fluid pumping. Compaction and cavitation must be coordinated with lineage specification for normal development of the embryo. Indeed, work in mice has revealed that establishment of polarity in the outer cells of the morula, subsequent to compaction, is necessary for lineage specification
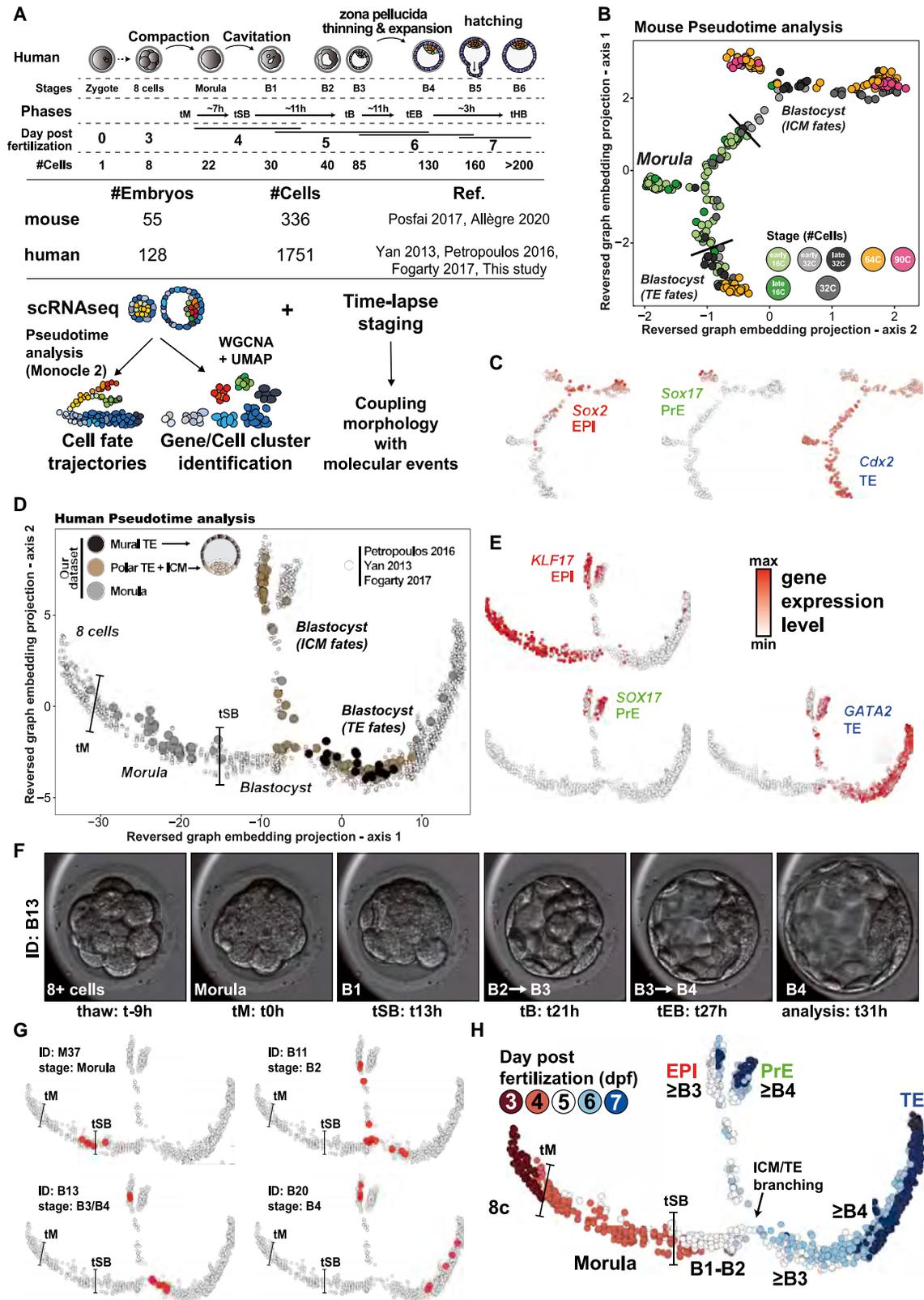
Figure 1. Pseudotime analysis of human and mouse pre-implantation embryo development

(A) Top: Schematic of human pre-implantation development, highlighting the link between developmental stages, morphological phases, dpf, and average number of cells observed. Center: summary of datasets used. Bottom: description of our experimental design. We used 2 mouse single-cell datasets and 4

(legend continued on next page)

(Hirate et al., 2013), and cavitation has been shown to be necessary for proper trophectoderm (TE) fate progression (Chan et al., 2019; Dumortier et al., 2019). Whether the regulation of morphogenesis is similar in human remains unclear.

Lineage specification in mice is considered to be driven by two sequential events. The first cell fate decision in the morula segregates the outer TE cells from inner cell mass (ICM) cells (White et al., 2018). Subsequently, in the blastocyst, ICM cells undergo a second cell fate decision to form the pluripotent epiblast (EPI) and primitive endoderm (PrE), precursors of the embryo proper and yolk sac, respectively (Chazaud et al., 2006). Whether this sequence is conserved in human embryos has been the subject of debate. On one hand, recent single-cell transcriptomics analysis of human pre-implantation embryos suggested simultaneous establishment of TE, EPI, and PrE lineages rather than a two-step model like in the mouse (Petropoulos et al., 2016). On the other hand, integrated analyses of several single-cell transcriptome studies of early human embryos supported the existence of an early human ICM molecular state, distinct from EPI and PrE, implying a two-step model, but could not definitively exclude the concurrent cell lineage specification model (Singh et al., 2019; Stirparo et al., 2018)

In the mouse, the first cell fate decision, segregating TE from ICM, occurs at the morula stage and is driven by a YAP/TEAD4/CDX2 axis (Chazaud and Yamanaka, 2016). Initially, outer cells are polarized and express aPKC and Amot, regulators of the Hippo pathway, at their apical membrane. In these outer polarized cells, the Hippo pathway permits Yap1 to translocate into the nucleus, where it binds to Tead4. The Yap/Tead4 complex activates TE fate drivers such as Cdx2, whereas non-polarized inner cells engage in an ICM fate.

A recent study showed that polarization/the Hippo pathway was involved in initiation of the TE fate in humans (Gerri et al., 2020). However, little is known regarding the progression of TE; CDX2 expression appears after cavitation in human embryos (Niakan and Eggan, 2013) and is therefore unlikely to be driving the TE fate as seen in the mouse. Only a few TE markers have been discovered in humans: GATA3, LAMA1, LAMA3, and KRT7 in hatched/post-implantation blastocysts; GATA2 in blastocysts after the B2/B3 stage, and CCR7 in polar TE cells (Aberkane et al., 2018; Deglincerti et al., 2016; Hannan et al., 2010; Kilens et al., 2018; Niakan and Eggan, 2013; Petropoulos et al., 2016; Shahbazi et al., 2016). Moreover, the molecular events that enable competent human blastocysts to interact with receptive luminal endometrium have remained largely elusive. An important observation is that human blastocysts attach to the endometrial surface epithelium from the polar side (Aberkane et al., 2018; Grewal et al., 2008; Lindenberg, 1991). This suggests that specific molecular events occur on the polar TE side of the blastocyst; however, the molecular events and underlying mechanisms remain to be identified.

The second cell fate decision, separating ICM cells into EPI and PrE, occurs at the blastocyst stage in the mouse. This second lineage specification is driven by a Nanog/Fgf4/Gata6 axis (Chazaud and Yamanaka, 2016). In EPI cells, Nanog induces Fgf4 secretion; Fgf4 induces Gata6 expression, and, in turn, Gata6 inhibits Nanog in those cells, yielding PrE-fated cells. In human embryos, GATA6-specific expression in PrE occurs upon implantation, whereas it occurs at the 90-cell blastocyst stage in the mouse (Deglincerti et al., 2016). Additionally, fibroblast growth factor (FGF) signaling does not seem to regulate EPI/PrE specification in humans (Kuijk et al., 2012; Roode et al., 2012). These results demonstrate differences from the mouse model. Single-cell RNA sequencing (scRNA-seq) studies have provided atlases of gene expression during human pre-implantation development, but it is still not clear whether and when cell fate decisions take place (Blakeley et al., 2015; Petropoulos et al., 2016; Singh et al., 2019; Yan et al., 2013). How distinct molecular regulators relate to specification of TE, EPI, and PrE lineages in humans remains to be elucidated.

In this study, we define the precise kinetics of gene expression and cell fate decisions during mouse and human early embryo development. We coupled morphological staging with molecular events, highlighting differences and similarities of mouse and human embryos. Last, we identify proteins that mark EPI, TE, and PrE fate progression. This study is a resource to study cell fate decisions during early human development.

RESULTS

Designing an experimental approach coupling fine staging with scRNA-seq analysis

One of the main difficulties when comparing mouse and human development is the differences in timing of development and the specificity of each developmental stage in each species. In the mouse, embryonic days are accurately linked to morphology and molecular events (Figure S1A). In humans, however, *in vitro* culture of embryos shows discrepancies between the timing of culture and morphology. Therefore, for humans, reproductive biologists rely on morphology-based annotation with precise criteria (Figure 1A; Alpha Scientists in Reproductive

---

human single-cells datasets to identify cell fate trajectories, resulting in a continuous transcriptomic pseudotime. We also performed co-expressed gene module identification with WGCNA, and a UMAP was performed on the activation score of the WGCNA module (module eigengenes) to map cell identities during pre-implantation development. Human embryos used for this study were imaged using a time-lapse microscope.

(B) Projection from the mouse scRNA-seq and single-cell qPCR (scqPCR) samples (Allègre et al., 2019; Posfai et al., 2017) from the reversed graph embedding method (Monocle2). Developmental stages are indicated as number of cells in the embryo.

(C) Projection of lineage marker expression levels on the mouse pseudotime: Sox2 (EPI), Cdx2 (TE), and Sox17 (PrE).

(D) Projection of stage and positional information for the samples we analyzed for this study, on the pseudotime. Morula cells (gray) and blastocyst dissection origin of cells are indicated (mural TE, black; polar TE or ICM, brown). tM, morula compaction; tSB, blastulation.

(E) Projection of lineage marker expression levels on the human pseudotime: KLF17 (EPI), SOX17 (PrE), and GATA2 (TE).

(F) Frames from time-lapse microscopy for embryo B13. For each embryo sequenced in this study, its morphokinetics were acquired using time-lapse microscopy. Developmental events include tM, tSB leading to the B1 stage, full blastocyst (tB) at the B3 stage, and expanded blastocyst when the *zona pellucida* thickness is halved (tEB) at the B4 stage. tM is used as t0 to compare thawed embryos.

(G) Projection of cells from 4 embryos, including embryo B13 (F), on the pseudotime.

(H) Projection of developmental day (3–7 dpf) for all samples combined for this study and the result of our refined staging.

Medicine and ESHRE Special Interest Group of Embryology, 2011). The numerous morphological events during the fifth day post fertilization (dpf) illustrate this: at 5 dpf, human embryos progress from early blastocyst (B1 and B2) to blastocyst (B3) and expanded blastocyst (B4) (Figure 1A). Molecular analysis must be linked to morphological staging to better understand human pre-implantation development.

Pseudotime analysis of scRNA-seq data appeared to be a good approach to study lineage specification and hierarchize molecular events. We used Monocle2 to generate developmental cell fate trajectories and identify the most likely path that temporally orders transcriptomics signatures of single cells (Qiu et al., 2017; Figure 1A). To identify lineage signatures, an essential benchmark for stem cell models, we clustered cells based on their transcriptomes. Finally, because we used embryos donated for research, staged carefully using time-lapse monitoring and *zona pellucida* thickness measurements (Feyeux et al., 2020) and graded according to clinical criteria, we were able to link embryo morphology with molecular events.

Transcriptomic pseudotime analysis of mouse and human pre-implantation development

We first computed the pseudotime of mouse pre-implantation embryo development using two existing datasets spanning early 16-cell morula to 90-cell stage blastocysts (Allègre et al., 2019; Posfai et al., 2017). Pseudotime analysis identified a common pool of progenitor cells that subsequently separates into two branches (Figure 1B). The pseudotime value indicates the level of transcriptomic change from the root cell (Figure S2B). Projecting the developmental stage annotations onto the pseudotime identified that the initial unspecified branch is composed mostly of cells from early 16-cell morula. Late 16-cell morula cells occupy the bifurcation point where cells make their first fate decision. Future cells, from early 32- and late 32-cell morula, occupy one of the two branches toward the ICM and TE fates. Cells from 64- and 90-cell blastocysts are located at the tips of specified branches of the pseudotime (Figure 1B). Enrichment of Sox2, Cdx2, and Sox17 expression allows identification of EPI, TE, and PrE branches, respectively (Frum et al., 2018; Figure 1C). Pseudotime analysis allowed us to reconstruct the developmental paths taken during early mouse embryo development, including the expected TE/ICM branchpoint as well as EPI/PrE bifurcation.

Having established the developmental pathways of early embryo cells in the mouse, we turned our focus to human embryos. We first generated scRNA-seq data of 25 human embryos from morula to B5 blastocysts (150 cells). We integrated our scRNA-seq dataset with available datasets (Fogarty et al., 2017; Petropoulos et al., 2016; Yan et al., 2013), resulting in an atlas of 1,751 cells from 128 embryos. Pseudotime analysis revealed 5 branches, with each branch containing samples from at least 2 datasets (Figure 1D; Figure S2A). Because our embryos were followed by time-lapse microscopy prior to scRNA-seq, we could univocally associate developmental stages for each embryo. Moreover, because blastocysts were laser dissected to physically separate the mural TE from the polar TE/ICM, we could also overlay positional information on the pseudotime (Figure 1D; Figures S1B–S1E). This revealed positioning of morula cells in the middle of the first branch of the pseudotime and the TE

branch as the longest branch extending on the right (Figure 1D). Projection of the expression levels of transcription factors suggested branches associated predominantly with EPI, PrE, and TE enriched for KLF17 (EPI), SOX17 (PrE), and GATA2 (TE), respectively (Figure 1E; Blakeley et al., 2015; Kilens et al., 2018; Niakan and Eggan, 2013; Xiang et al., 2020).

To link developmental stage and molecular events, we performed a per-embryo analysis in which cells from the same embryo were analyzed together. We then regrouped embryos based on their position on the pseudotime (Figure S2C). Sample images are shown for blastocyst ID 13 (B4 stage upon scRNA-seq analysis) (Figure 1F). We projected all cells from our cohort of embryos on the pseudotime, linking embryo annotation to the pseudotime (Figure 1G; Figure S2C). Our precise annotation showed that, in humans, TE and ICM cells become transcriptionally distinct between the B2 and B3 stages, after the beginning of blastocyst cavitation (Figure 1H; Figure S2C). These results were in stark contrast to mouse embryos, where branching between ICM and TE fate occurred earlier, between the 16- and 32-cell morula stage (Figure 1B). Our results suggest that, in human embryos, ICM cells are transcriptionally distinct from TE cells shortly after formation of the blastocyst, unlike in the mouse, where this event takes place earlier.

Defining the hierarchy of gene expression and lineage signature during human pre-implantation development

The next step was to define lineages associated with each cell. Pseudotime analysis is particularly suited to studying pre-implantation development as a dynamic process. We used WGCNA (weighted gene co-expression network analysis) (Langfelder and Horvath, 2008) to identify gene expression signatures associated with distinct developmental stages and lineages. Gene module activation or repression can be summarized by a linear combination of gene expression values called module eigengenes. To produce precise mapping of transcriptome identity, we used module eigengenes from gene modules reduced in two dimensions by a UMAP (uniform manifold approximation and projection) approach (McInnes et al., 2018). Finally, we clustered cells based on their relative position on the UMAP (Ester et al., 1996). This featured 8 major clusters indicative of specific lineages and stages; we qualified cells located between clusters as undefined or "intermediates" (Figure 2A; Figure S3).

Module eigengenes classify EPI, PrE, and TE cells in an unsupervised manner. In contrast to Petropoulos et al. (2016), who used successive rounds of principal-component analysis (PCA) to identify different cell types and loadings to identify the associated markers, our method gives a more confined identification of PrE and a refined association of fates with developmental stages and also identifies cells that are undefined or intermediates, limiting the noise in the fate-associated signatures (Figure S4A). Stirparo et al. (2018) classified embryonic day 5 (E5) non-TE cells as ICM. The majority of the cells they identified as ICM are within our EPI cluster (Figure S4B). We did not identify a stringent population of unspecified cells that could be considered a proper ICM cluster. However, our analysis highlighted 3 clusters of unspecified cells and subdivided the TE cells into 3 subclusters based on their progression on the pseudotime (Figure 2B). Our unsupervised analysis therefore identified developmental molecular states during pre-implantation development and
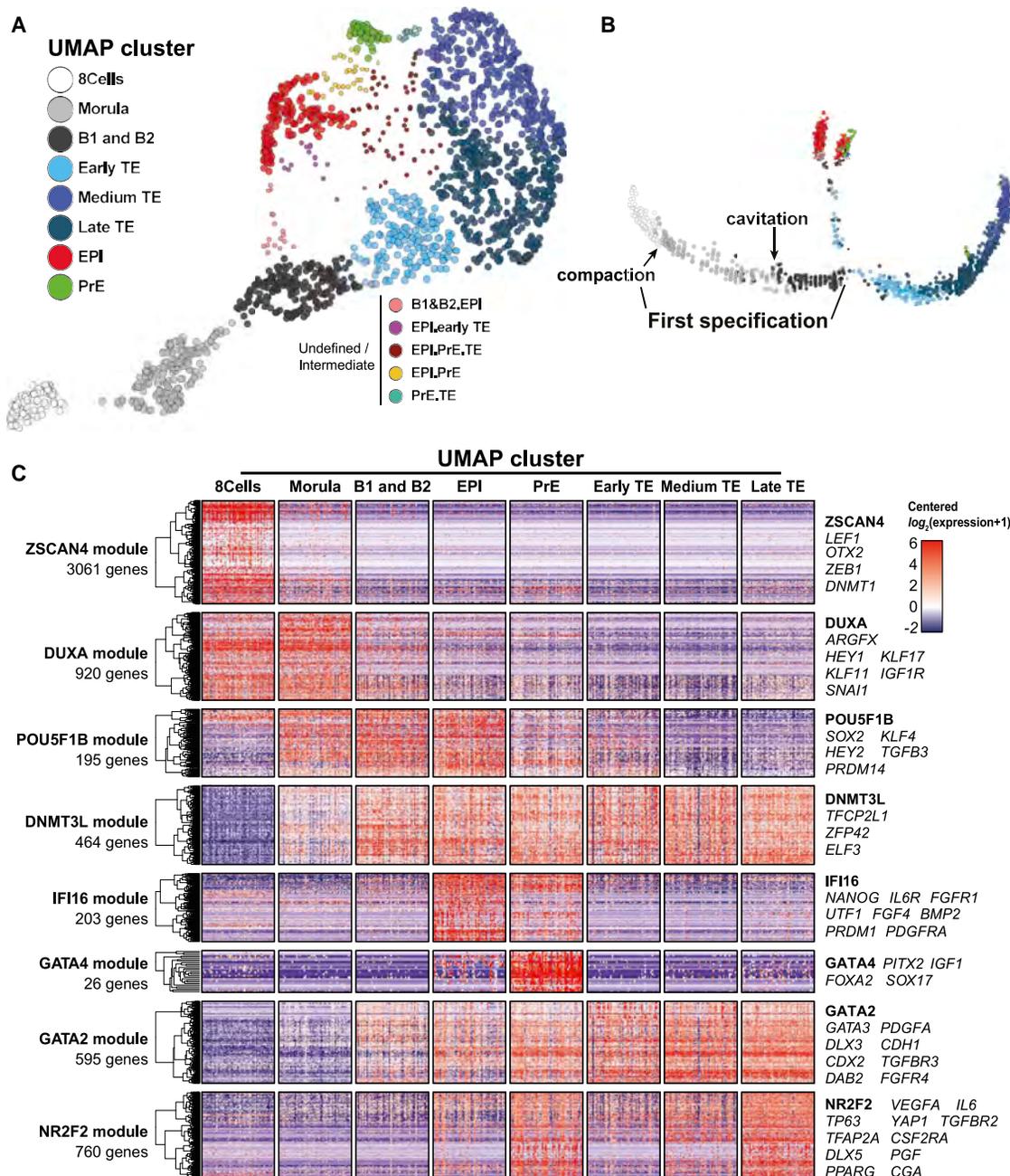
Figure 2. Gene modules define cell fate transcriptional signatures, and pseudotime indicates the hierarchy of events

(A) Dimension reduction (UMAP) of WGCNA module eigengenes, colored by density-based clusters. Small dots indicate a minor cluster composed by the intermediate transcriptome. Medium TE and late TE were segregated by additional k-means clustering based on NR2F2 and GATA2 module eigengenes.

(B) Projection of density-based clusters from (A) on the pseudotime.

(C) Expression heatmap of all genes related to WGCNA modules. Each row represents a WGCNA module, and each column is a set of 50 cells drawn from a UMAP cluster (A). The height of each row represents the number of genes in the corresponding WGCNA module following a log scale. For each module, a set of genes belonging to the module is indicated on the right side of the heatmap.

provides an alternative, refined cellular annotation of cell fate lineages in the early human embryo.

To further analyze the temporal dynamics of gene expression during human pre-implantation development, we matched gene module expression with each cluster of cells obtained with the UMAP (Figure 2C). This revealed unique behavior of 8 modules

of genes, named after a representative gene (Figure S3). The 3 clusters of unspecified cells are distinguished based on expression of (1) the ZSCAN4 module, exclusively within 8-cell stage embryos; (2) the DUXA module and onset of the POU5F1B and DNMT3L modules in morula cells; and (3) absence of the ZSCAN4 module, fading of the DUXA modules, and the presence
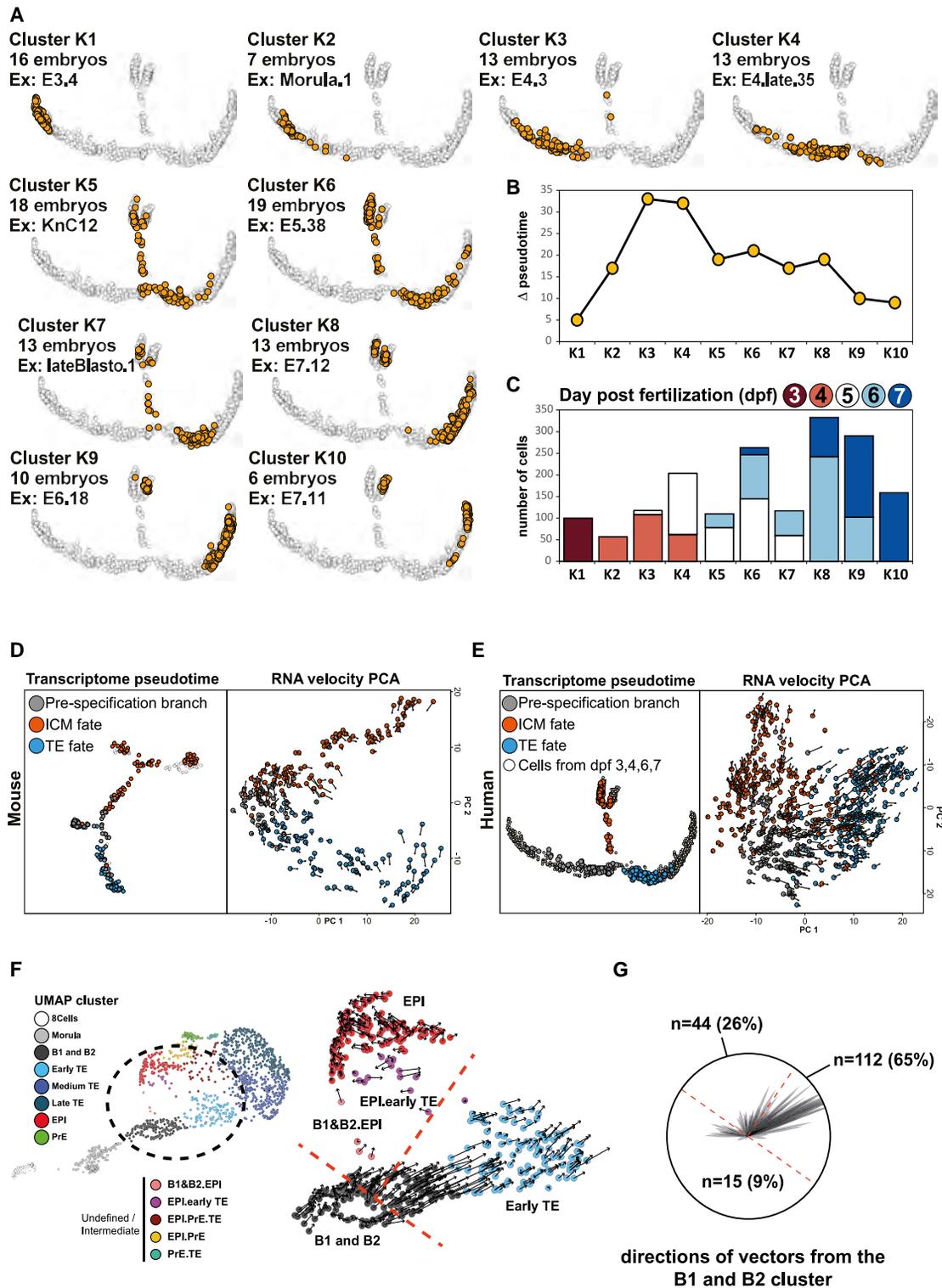
Figure 3. Early blastocysts contain a heterogeneous cell population that is preparing to specify despite having similar transcriptomes

(A) Projection of each embryo cluster (k-means) according to the position of its cells on the pseudotime. For each embryo cluster, the corresponding number of embryos and a representative embryo are indicated. Clusters are ordered by their mean pseudotime.

(B) Range of pseudotime values per embryo cluster.

(C) Distribution of number of cells per embryo cluster subdivided by dpf.

(D) Transcriptome pseudotime and RNA velocity comparison of cells before and after specification in the mouse.

(E) Transcriptome pseudotime and RNA velocity comparison of cells before and after specification in humans.

(legend continued on next page)

of the POU5F1B/DNMT3L modules in early blastocysts (Figure 2C; Figure S4C). Regarding TE cells, 3 states emerge from the pseudotime analysis: (1) a cluster expressing the GATA2, POU5F1B, and DNMT3L modules that we called early TE; (2) a cluster expressing the GATA2 module but not POU5F1B; and (3) a cluster expressing the GATA2 and NR2F2 modules (Figure 2C; Figure S4C). These analyses defined distinct modules of genes whose dynamic expression characterizes early human embryo development.

The dynamic expression pattern of modules within clusters and pseudotime inform on the potential role of genes in each module. Some modules are not associated with fates but reflect overall changes in embryo development. For example, the ZSCAN4 and DUXA modules are associated with zygotic genome activation between the 8-cell and morula stages, whereas the DNMT3L module is emerging in all cells at the blastocyst stage and contains epigenetic regulators, in line with methylation dynamics in human pre-implantation development and metabolic pathways (Figure S4D; Greenberg and Bourc'his, 2019). On the other hand, some modules are associated with fates and are expressed sequentially. The POU5F1B module, containing pluripotency genes, is first detected in all cells of the morula and B1 and B2 blastocysts and is then maintained in the EPI but reduced in the PrE and TE. Consequently, the POU5F1B module is the first module that goes through a process of global to restricted lineage-specific expression in more developed embryos (Figure 2C). Other modules are related to specific lineages; for example, the IFI16 module for developed/stable EPI, the GATA4 module for PrE, the GATA2 module for early TE/medium TE/late TE, and the NR2F2 module for late TE. Expression of several genes within lineage-specific modules aligns with the current understanding of developmental expression dynamics. For example, the IFI16 module contains NANOG and overlaps with expression of the POU5F1B module in B4 blastocysts (Figure 2C). The GATA4 module contains the characterized regulators of PrE fate SOX17 and FOXA2. Our dual analysis by pseudotime and gene correlation allowed us to hierarchize states emerging during pre-implantation development, linking them with developmental stages (Figure S4C). This highlights how our analysis can be used to refine human pre-implantation studies by serving as a reference for developmental stages and progression of molecular signatures that lead to specification. All annotations and expression profiles can be found in a user-friendly online browser we generated to facilitate access to human and mouse pre-implantation datasets (Figure S4E).

Human morula and B1/B2 blastocyst cells show heterogeneity

Our pseudotime analysis, combined with time-lapse imaging of embryos, suggests that embryo cells are transcriptionally different after human cavitation. To refine this conclusion, we studied transcriptional heterogeneity within each embryo by clustering embryos based on their individual position on the

pseudotime. Cells belonging to each embryo can only belong to one cluster. We then measured the pseudotime spreading of each cluster because it reflects transcriptional variability, and reported annotations associated with embryos from each cluster. For example, cluster 1 spans a relatively short pseudotime distance and contains only 3-dpf embryos (Figure 3A). Clusters K3 and K4 have the highest pseudotime distance variation (Figure 3B). Interestingly, cluster K3 contains mostly 4-dpf embryos, suggesting that, within human morula, some cells develop faster (Figure 3C).

To test whether morula cells, located just prior to the first pseudotime bifurcation, have already initiated a transcriptional program biased toward a fate, we used RNA velocity, a measurement of non-spliced mRNA that infers cellular fate (La Manno et al., 2018). In the mouse, RNA velocity analysis of transcriptionally similar cells showed that cells had a velocity trending toward ICM or TE (Figure 3D). Thus, at the 16-cell stage, mouse cells are biased toward TE or ICM, but the transcriptomic (mRNA) differences are mostly visible at the 32-cell morula stage (Figure 3D; Jedrusik et al., 2008). Similarly, in humans, RNA velocity showed that, despite having similar mRNA profiles, unspecified cells localized on the pseudotime prior to branching are already biased toward ICM or TE fates, in agreement with mouse work (Graham and Zernicka-Goetz, 2016; Figure 3E). This can be observed when projecting the velocity vectors on the UMAP cluster B1/B2 (Figures 3F and 3G). Heterogeneity in human embryos seemed to be established at the morula stage, but inner and outer cells are not transcriptionally distinct until the B3 blastocyst stage.

Identification of markers of compaction and cavitation during human pre-implantation development

Compaction of cells at the morula stage requires establishment of apico-basal polarity. In the mouse, compaction is initiated or characterized by sequential establishment of adherent junctions, marked by CDH1, followed by establishment of tight junctions, marked by ZO1 (Barcroft et al., 1998, 2003; White et al., 2018). To refine our pseudotime, we investigated establishment of apico-basal polarity in human embryos. Immunostaining of ZO1 and CDH1 during human pre-implantation development showed basolateral expression of CDH1 from the morula stage, with subsequent apical recruitment of ZO1 (Figure 4A). This supports the theory that apico-basal polarity in human embryos is linked to molecular events, similar to other mammalian species (Gerri et al., 2020; Reijo Pera and Prezzoto, 2016).

After acquisition of apico-basal polarity and compaction, an important event in mammalian pre-implantation development is formation of a blastocoel cavity (White et al., 2018). This is mediated by expression of aquaporins at the morula/early blastocyst stage (Barcroft et al., 2003; Xiong et al., 2013). AQP3 is the main water channel expressed during human pre-implantation development and is one of the few genes that are initially expressed in all cells but then restricted to TE. Immunostaining

---

(F) RNA velocity vectors projected on the B1 and B2, B1&B2.EPI, EPI, EPI.early TE, and early TE clusters from the UMAP analysis. Cells are colored by cell clusters.

(G) Summary of the direction and magnitude of RNA velocity vector of the B1 and B2 cell cluster by a circular diagram. Each represented vector has an opacity of 20% to represent an estimation of vector density. 114 vectors of 171 are in a sector of 45° of the diagram that is facing the Early TE cluster, and 42 are facing the EPI cluster. The sectors are represented by a dashed orange line.

A

B
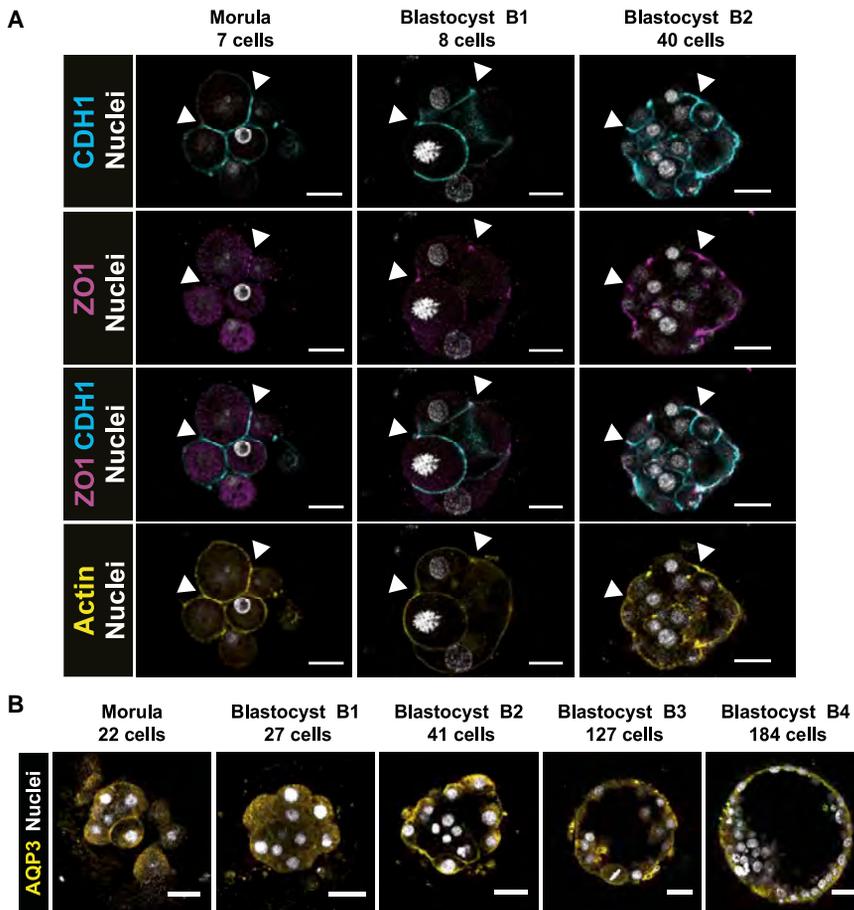
Figure 4. Polarization of outer cells of the morula precedes restriction of the TE marker AQP3

(A) IF of CDH1 (cyan), ZO1 (purple), Actin (yellow), and nuclear counterstaining (white) at the indicated stages. An arrowhead points to the apical part of the cell, with ZO1 staining next to CDH1 staining (n = 3).

(B) IF of AQP3 (yellow) and DAPI (white) as a nuclear counterstain at the indicated developmental stages (n = 6).

Scale bars, 47 μm.

To further understand IFI16 dynamics within the human ICM, we performed co-staining with NANOG and GATA4, which are mutually exclusive in expanded blastocysts (Figure 5C; Roode et al., 2012). In B4 and B5 embryos, IFI16 co-localized with NANOG (EPI)-positive cells or with GATA4 (PrE)-positive cells. To clarify whether IFI16 was restricted to EPI and/or PrE upon their maturation, we extended our analysis to later developmental time points. We used a recently established *in vitro* culture protocol to simulate implantation (Deglincerti et al., 2016; Shahbazi et al., 2016). Here B3 or B4 embryos were cultured for 72 h *in vitro*, which is considered equivalent to "day 8" human embryos. We observed NANOG-positive cells that clearly expressed IFI16, whereas GATA4-positive cells were IFI16 negative or expressed IFI16 weakly (Figure 5D). Quantification of immunofluorescence in pre-implantation embryos and B3 or B4 embryos cultured for 72 h *in vitro* suggests that, before implantation, ICM cells broadly express IFI16, whereas after implantation, cells expressing high levels of IFI16 are negative for GATA4 (Figures 5E and 5F).

for AQP3 revealed cytoplasmic membrane localization at the morula stage before being restricted apically at the B2 stage (Figure 4B). Loss of AQP3 in the ICM at the B2 blastocyst stage could therefore indicate onset of a program linked to the ICM, consistent with our pseudotime analysis.

These results allowed us to place the major morphogenesis events, compaction and cavitation, on the unspecified branch of the pseudotime (Figure 2D). CDH1, ZO1, and AQP3 can therefore be used as markers to identify molecular progression of human embryos.

IFI16 and GATA4 highlight progression of EPI and PrE specification

Currently, the number of markers used to study EPI/PrE lineage specification in human is limited. In particular, we need markers that allow us to track progression of cells within EPI or PrE fates. Using our integrated transcriptomics analysis, we sought to identify markers of developed EPI in B5 hatching blastocyst. Among transcription factors, we focused on IFI16 as a candidate for developed EPI. We analyzed protein expression of IFI16 in B5 embryos, which showed IFI16-positive staining restricted to ICM cells, in contrast to GATA2 expression in TE cells (Figure 5A). IFI16 was not detected before B2 and was robustly detected after B4 in ICM cells (Figure 5B). These results are consistent with previous transcriptional analyses suggesting a link between IFI16 and EPI (Boroviak et al., 2018).

We found that IFI16 is restricted to EPI post-implantation in human embryos. Loss of IFI16 might therefore indicate advancement toward the PrE fate. This observation raised an interesting hypothesis: PrE could be specified later than EPI in humans (EPI and PrE are linked differentially to dpf; linear regression, p = 1.51×10^{-12}; Figure S5A). The difficulty to identify a distinct ICM molecular signature that would correspond to progenitors of EPI and PrE like in the mouse might indicate that EPI and ICM molecular fates in humans are highly similar or that PrE in humans differentiates from EPI. To better understand PrE fate, we analyzed a recent scRNA-seq dataset of human embryos cultured up to 120 h (day 5) and then switched to IVC medium for up to 216 h (day 14) (Zhou et al., 2019). We focused our analysis on day 5 + 24 h and day 5 + 72 h prolonged culture. UMAP showed that EPI and PrE cells were more related to each other (closer) at day 5 + 24 h than at day 5 + 72 h (Figures S5E and S5G). Interestingly, day 5 + 24 h embryos had cells co-expressing *IFI16* and *GATA4*, whereas this was not the case in day 5 + 72 h embryos (Figures S5F and S5H). We completed this analysis
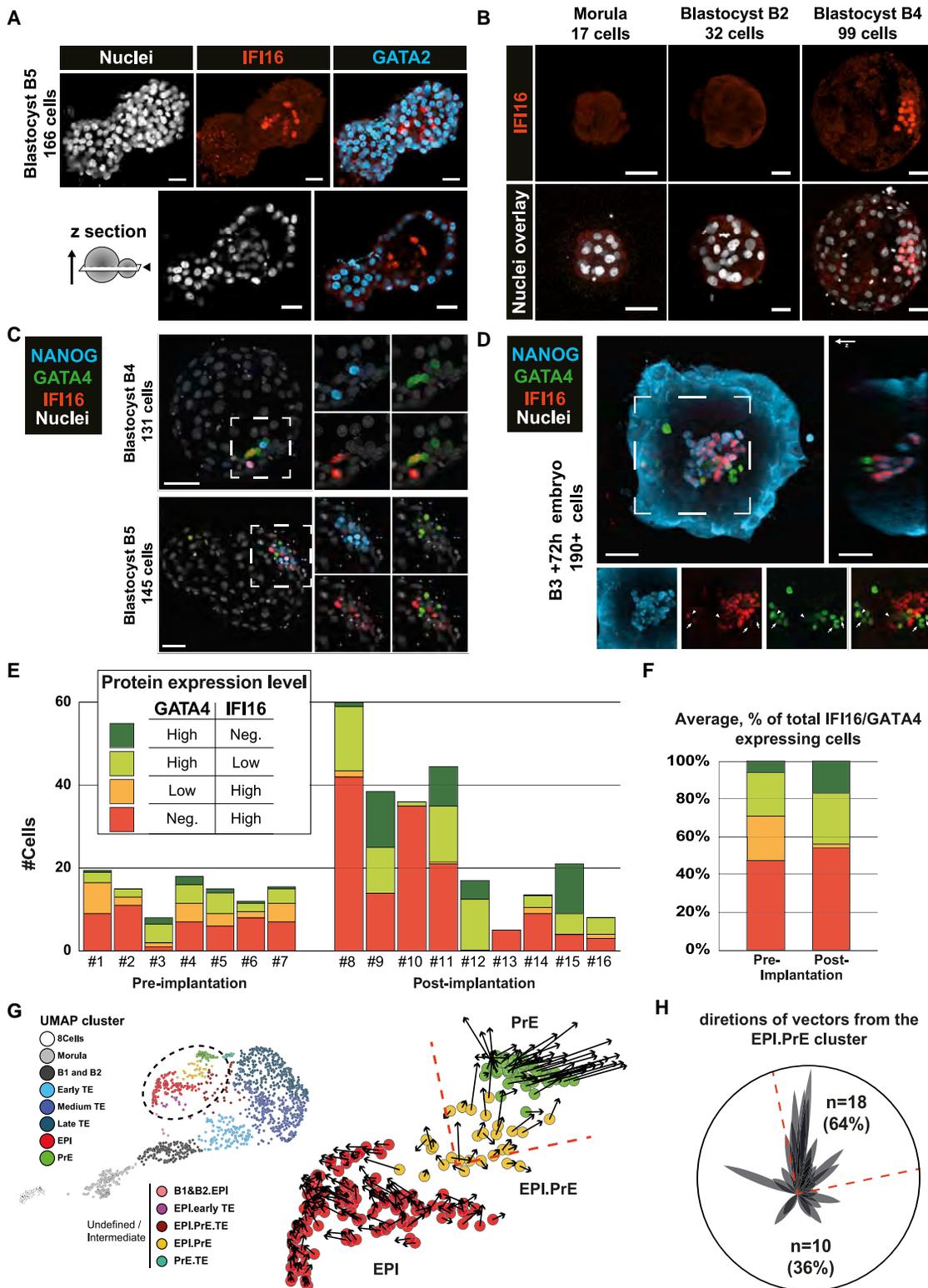
Figure 5. NANOG/IFI16/GATA4 dynamics highlight progression of EPI/PrE specification

(A) IF of IFI16 (red) and GATA2 (cyan) at the B5 blastocyst stage. The z section indicates a z cutting plane (n = 3).

(B) IF of IFI16 at the indicated stages. Nuclear counterstaining is white (n = 13).

(C) IF of NANOG (cyan), GATA4 (green), and IFI16 (red) at the indicated stages. Nuclear counterstaining is white (n = 3).

(D) IF of NANOG (cyan), GATA4 (green), and IFI16 (red) in a B3 + 72 h attached embryo. Arrow, GATA4$^+$/IFI16$^+$ cell. Arrowhead, GATA4$^+$/IFI16$^-$ cell (n = 4).

(legend continued on next page)

by projected velocity vectors on the UMAP from our dataset or the post-implantation dataset (Figures 5G and 5H; Figures S5E and S5F). The vectors show that, at late blastocyst stage, some EPI cells show a shift toward PrE gene expression. This further supports our hypothesis that PrE specification initiates at the B4 stage and that PrE might differentiate from cells that are transcriptionally close to EPI in humans. Further analysis is required at the B3 stage to identify the molecular states of cells that would eventually become PrE.

To further validate our observations, we investigated expression of another marker: OTX2. OTX2 is an EPI-associated lineage marker in mouse embryos (Acampora et al., 2016; Buecker et al., 2014; Shahbazi et al., 2017) but has been linked to PrE in humans (Boroviak et al., 2018; Zhou et al., 2019). In pre- and post-implantation embryos, we observed that OTX2 only co-localized with GATA4-positive cells and is not expressed in NANOG-positive cells (Figures S5B–S5D). Interestingly, in day 8 embryos, OTX2 was expressed in GATA4-positive cells closer to NANOG-positive cells (Figures S5B–S5D). It remains to be defined whether OTX2 indicates more advanced PrE development or a different subset of PrE.

Our transcriptomic analyses, validated by immunofluorescence (IF), support that EPI/PrE specification in humans occurs in B4 (late) blastocysts, which is different from the mouse, where EPI and PrE fates are established in 90-cell (early) blastocysts.

NR2F2 marks TE maturation at the polar side of human embryos

We next sought to decipher the maturation events in the TE branch. A transcription factor of interest was NR2F2 because of its expression in the later part of the TE branch, which corresponds to developmental stages of expanded/hatched blastocysts (B4 and thereafter; Figures S3A and S3B). In B5 blastocysts, IF showed that nuclear localization of NR2F2 was restricted to polar TE cells juxtaposed to EPI cells, expressing NANOG (Figure 6A). We then investigated NR2F2 expression in B4 blastocysts. Immunostaining revealed GATA3 and GATA2 expression throughout TE, whereas NR2F2 was only expressed in the subset of polar TE cells (Figure 6B). The pseudotime analysis indicates that NR2F2-expressing cells are the most mature because they are at the end of the trajectory. However, IF analysis showed expression of NR2F2 in B4 embryos, and B4 TE cells are generally localized in the middle of the TE branch of the pseudotime (Figure S2C). This suggests that maturation of TE is initiated on the polar side by an EPI-TE dialog.

To further characterize onset of NR2F2$^+$ cells, we co-stained NR2F2 with markers of EPI (IFI16) and PrE specification (GATA4). This revealed that NR2F2 expression is concomitant with IFI16 and GATA4 expression (Figure 6C; Figure S6). Staining of NR2F2 in B3/B4 + 72 h *in vitro* cultured embryos confirmed

spreading of NR2F2 to all TE cells (Figure 6D). We therefore propose that maturation of TE is initiated by contact with EPI and then spreads upon implantation.

The observation that maturation of TE cells is initiated at the polar side is consistent with the observation that the majority of human blastocysts are attached to endometrial cells by the polar side with subsequent spreading of TE development to mural cells (Aberkane et al., 2018; Bentin-Ley et al., 2000; Grewal et al., 2008; Lindenberg, 1991). We grouped cells as NR2F2$^+$ and NR2F2$^-$ to highlight pathways specific to polar TE. This revealed pathways for which the receptor is on NR2F2$^+$ polar TE cells (i.e., GM-CSFR), and the ligand is secreted by the endometrium (i.e., GM-CSF) (Giacomini et al., 1995; Ziebe et al., 2013). Analysis of the most enriched signaling pathways with fGSEA (Korotkevich et al., 2019) identified prime candidates potentially driving the molecular dialog from EPI toward TE, such as transforming growth factor β (TGF-β), insulin growth factor 1 (IGF1), BMP2, and FGF4, and from TE toward EPI, such as platelet-derived growth factor (PDGF), interleukin-6 (IL-6), and WNT (Figure S7; Figure 6E). This suggests that FGF4 might still have a role in pre-implantation development despite being ruled out from regulating PrE specification (Kuijk et al., 2012; Roode et al., 2012). BMP signaling has been shown recently to inhibit cavitation (De Paepe et al., 2019), but its function after the first lineage specification remains to be studied. The role of IL-6 has been studied recently in pigs; IL-6 knockout (KO) or inhibition of JAK signaling perturbed pre-implantation development, supporting the hypothesis that, in humans and pigs, in the absence of LIF, JAK/STAT signaling is triggered by IL-6 (Ramos-Ibeas et al., 2019). Polar TE-EPI interactions in humans is reminiscent of the ICM-polar TE molecular dialog observed in mouse blastoids (Rivron et al., 2018). Mouse blastoids showed that EPI is necessary for proper TE maturation. However, human-specific events might be involved because some genes critical for mouse TE maturation are not restricted to TE in humans, such as KLF6 (Rivron et al., 2018).

We found that NR2F2 marks mature TE in B4 expanded blastocyst and spreads to all TE cells. Identification of NR2F2$^+$ cells will give rise to numerous hypothesis regarding the dual molecular dialog between polar TE and the EPI and endometrium.

DISCUSSION

We generated continuous mouse and human pre-implantation embryo transcriptome atlases by implementing lineage reconstruction approaches from scRNA-seq data. The pseudotime-ordered transcriptomic mouse trajectory corroborates existing functional experiments (Chazaud and Yamanaka, 2016; Posfai et al., 2017). For example, cells become transcriptionally distinct at the early 32-cell stage, immediately after differential Cdx2

(E) Manual counting of GATA4-high/IFI16$^-$, GATA4-high/IFI16-low, GATA4-low/IFI16-high, and IFI16-high/GATA4$^-$ cells in pre-implantation and post-implantation embryos.
(F) Average percentage of total IFI16/GATA4 expressing cells in pre- and post-implantation embryos.
Scale bars, 47 μm.
(G) RNA velocity vectors projected on the EPI, EPI.PrE, and PrE clusters from the UMAP analysis. Cells are colored by cell clusters.
(H) Summary of the direction and magnitude of RNA velocity vectors of the EPI.PrE cell cluster by a circular diagram. Each represented vector has an opacity of 45% to represent an estimation of vector density. 18 vectors of 28 are oriented within an angle of 45° in the direction of the PrE cluster (p ≈ 2.21.10^{-6}, obtained from the binomial distribution of parameter p = 0.25 and n = 28). The sectors are represented by dashed orange lines.
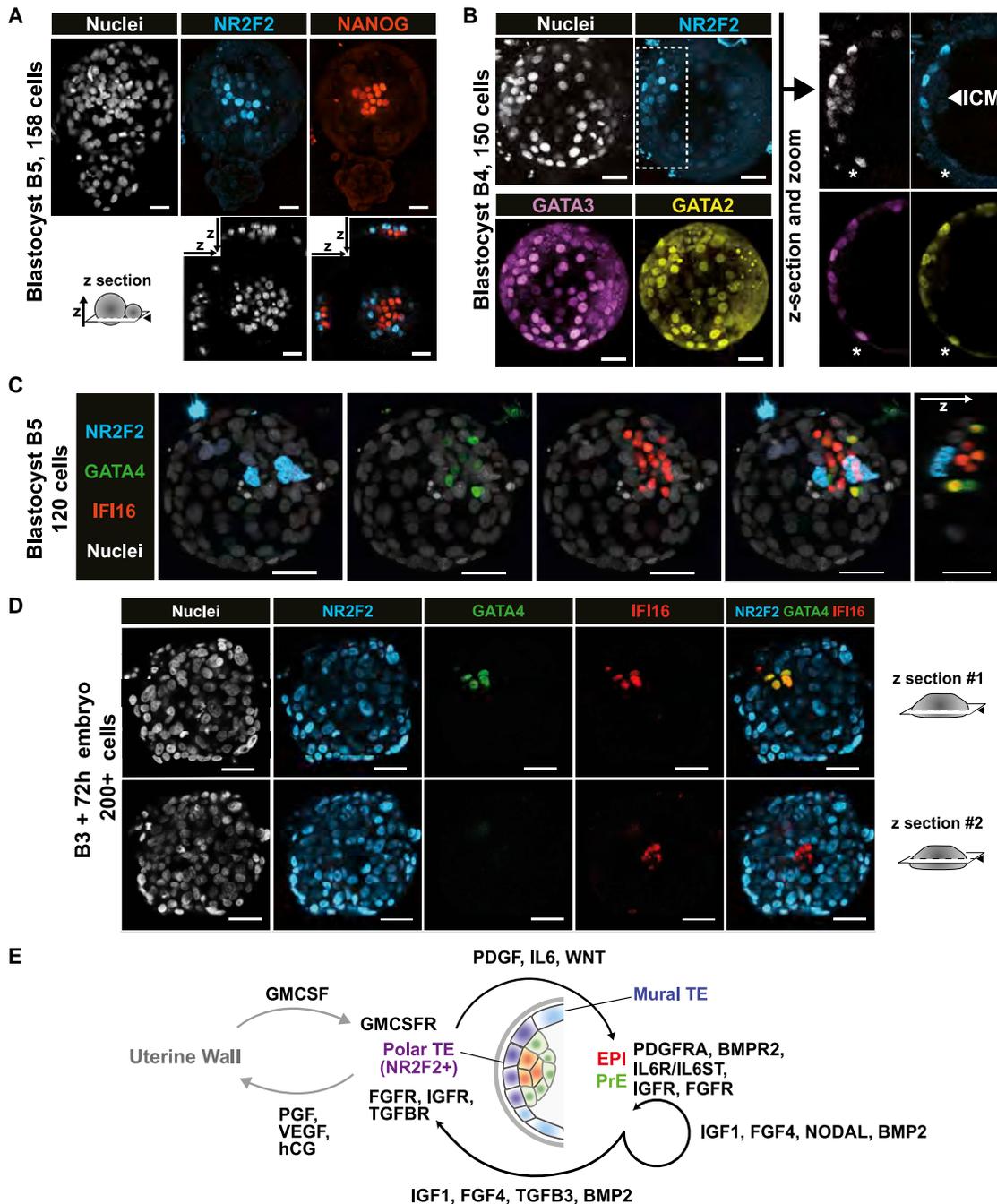
Figure 6. NR2F2 reveals differential maturation of polar and mural TE

(A and B) IF of NR2F2 (cyan) and NANOG (red) at the B5 stage (A) or with GATA2 (yellow) and GATA3 (purple) at the B4 stage (B). Asterisks mark cells that are negative for NR2F2 and positive for GATA3/GATA2 (n = 3).

(C) IF of NR2F2 (cyan), GATA4 (green), and IFI16 (red). Nuclear counterstaining (DAPI) is white (n = 4).

(D) IF of NR2F2 (cyan), GATA4 (green), and IFI16 (red) after 72 h of prolonged culture of a B3 blastocyst (n = 3). Scale bars, 47 μm.

(E) Schematic representing identified cytokine-receptor loops.

protein expression at the late 16-cell morula stage. Experimentally, mouse TE cells at the 32-cell stage are committed, whereas ICM cells may be specified but not yet committed (Grabarek et al., 2012; Handyside, 1978; Rossant and Lis, 1979). The human pseudotime analysis shows the precise timing of transcriptionally distinct TE at the transition from the B2 to the B3 stage. Our embryo-per-embryo analysis strategy revealed that transcriptomic heterogeneity could be found in human morula prior to complete segregation of cells into either of the two lineages. Coupling pseudotime with gene correlation analysis revealed the dynamics of
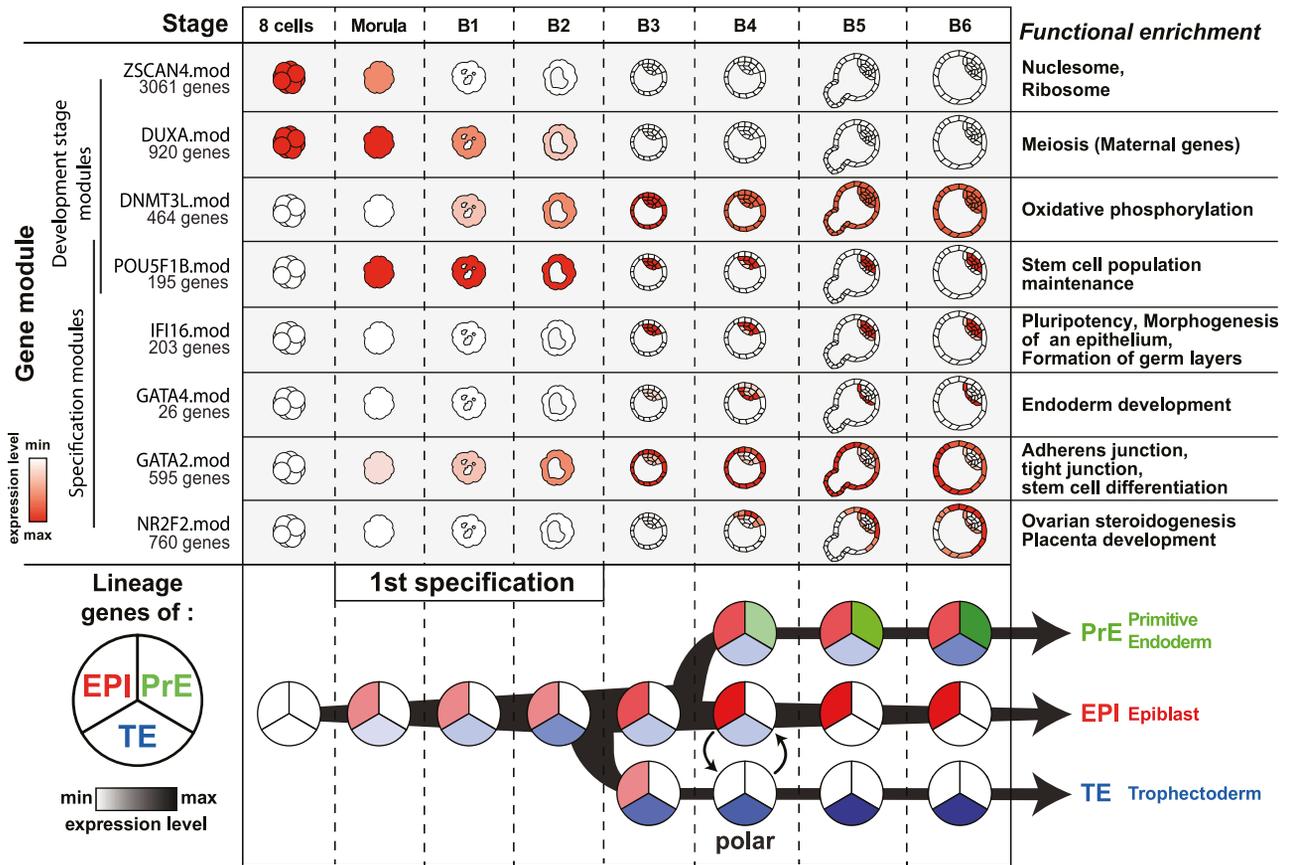
Figure 7. Human pre-implantation development model
Each annotation is represented according to morphology-based stages of human pre-implantation development. Top: schematic representation of gene module global expression. Terms highlighted by functional enrichment are presented on the right. Complete enrichment data are presented in Figure S4D. Bottom: expression of lineage-specific stage per stage and per cell fate.

several gene modules that could be associated with specific states within each branch of the pseudotime. This led us to reveal, by IF, that IFI16 is expressed in a majority of ICM cells at the B4 stage, and progressively fades in the developing PrE cells. Moreover, we discovered that maturation of TE was initiated on the polar side, adjacent to the EPI, which yielded a molecular dialog. Our study improves our understanding of the molecular events occurring during human lineage specification and provides new markers of specific developmental steps (Figure 7).

Human in vitro pre-implantation development is highly heterogeneous from one embryo to another. The best way to annotate embryo stages to date is to record the development of human embryos with time-lapse devices (Apter et al., 2020). Combination of our scRNA-seq analysis of time-lapse annotated human embryos with previous datasets resolved annotation overlap between 4, 5, and 6 dpf, which previously limited translation of those datasets into a sequence of events, pacing human pre-implantation development. Indeed, binning embryos at 5 dpf results in averaging of transcriptome information from cavitating B1 blastocysts to B4 expanded blastocysts. Because the TE, PrE, and EPI transcriptomes are emerging in that time frame, binning it all together creates a lot of noise in subsequent analyses. Our analysis, combining time-lapse annotation and

scRNA-seq, improves our ability to generate hypotheses regarding the molecular events regulating human pre-implantation development.

Two morphogenic events are particularly noticeable during mammalian pre-implantation development: compaction and cavitation. Compaction seems to involve rapid epithelialization in mouse and human (White et al., 2018). Gerri et al. (2020) showed that compaction coupled to the Hippo pathway triggers initiation of TE fate at the morula/B1 stage, which is characterized by expression of GATA3 in external cells. We found that transcriptional variability was increased greatly between cells from the morula but without achieving fate-associated transcriptomic signatures. The delay in the onset of distinct transcriptomic profiles of TE/ICM in humans compared with the mouse is rather surprising. This observation suggests that, in addition to compaction, other parameters are likely required to induce/complete lineage specification. One of these could be cell division. Human morulae compact at 10 cells and cavitate at 20 cells, resulting in a B1 stage that rapidly evolves to B2 stage blastocysts, generally composed of 40 cells. This suggests that two rounds of cellular division, after compaction, are required before cells can initiate/complete distinct transcriptomic programs relating to the ICM/TE. This occurs similarly but slightly earlier

in mouse development, where cell compaction takes place at the 8-cell stage and emergence of distinct cellular profiles is first seen at the 32-cell stage. Regarding cavitation, our analysis also revealed expression of AQP3, which was restricted to TE cells at the B2 stage. However, it remains to be demonstrated whether AQP3 expression depends on TE fate regulators or whether TE fate regulators depend on AQP3.

EPI/PrE specification is difficult to resolve in humans regardless of the approaches used (Blakeley et al., 2015; Petropoulos et al., 2016; Stirparo et al., 2018). Our analysis suggests that, within the ICM, the EPI fate is the first to be achieved. Computational modeling of the mouse raised similar conclusions: EPI cells need to secrete Fgf4 for PrE cells to specify (De Mot et al., 2016). Regarding PrE fate, we found that the PrE signature is defined better when analyses include embryos in prolonged culture; day 6 embryos cultured in IVC medium seem to have more developed PrE cells than day 6 embryos cultured in IVF medium (Petropoulos et al., 2016; Zhou et al., 2019). This could be because IVF media are not currently designed to support extended culture of embryos. It has been determined that day 7 blastocyst were less likely to implant (Shoukir et al., 1998) and are only transferred when no other embryos are available (Tiegs et al., 2019). Another possibility is that IVC medium favors rapid growth/development of human embryos. This observation shows how important it is to understand pre-implantation development in humans to improve embryo culture media.

We consider two main hypotheses for the EPI/PrE specification in humans: (1) early ICM cells are transcriptionally closer to EPI than to PrE or TE, resulting in ICM cells clustering with EPI cells; (2) PrE differentiates from EPI. More experiments are necessary to solve these hypotheses, but our study provides a framework; we have pinpointed the morphology associated with specific marker expression and provide novel markers informative of EPI/PrE specification, such as IFI16 and GATA4. In particular, IFI16 characterizes the transition between molecular states during EPI and PrE peri-implantation development. IFI16 expression suggests that IFNg signaling might be important for EPI specification. Furthermore, IFI16 has been shown to induce epigenetic silencing of viral promoters in immune cells (Roy et al., 2019). Therefore, one hypothesis is that IFI16 might inhibit the burst of transposable elements expressed at the morula stage (Giocanti-Auregan et al., 2016; Theunissen et al., 2016). Shutting down transposable elements might be necessary for EPI/PrE specification.

Transcriptomically, TE acquires a distinct expression profile at the transition from the B2 to the B3 stage, with cells progressively losing expression of pluripotency-associated genes, correlating with loss of plasticity of TE cells (De Paepe et al., 2013). We provide evidence showing that an EPI/TE molecular dialog could be involved in TE maturation. Interestingly, it is TE cells adjacent to the EPI, on the polar side, that typically initiate implantation prior to maturation of the remaining mural TE cells. However, in mouse embryos, secretion of Fgf4 and nodal by EPI contributes to the progression of polar and mural TE fates, and attachment is mediated by the mural, mature TE cells, highlighting differences between the two species (Guzman-Ayala et al., 2004; Yamagata and Yamazaki, 1991). It will be interesting to understand what triggers maturation of TE and whether NR2F2 plays a central role in this process in the mouse and humans.

Studies have demonstrated the importance of TE morphological quality for prediction of successful IVF (Ahlström et al., 2011; Chen et al., 2014; Hill et al., 2013; Thompson et al., 2013). Therefore, understanding this aspect of human pre-implantation development is of utmost importance to improve of IVF. We will now be able to focus on specific secreted markers associated with NR2F2$^+$ cells that could inform clinicians about the implantation potential of the blastocyst before transfer. Indeed, secreted markers that correlate with expression of NR2F2 could be predictive of the implantation capacity of embryos. This discovery will support the much needed hypothesis regarding human implantation and complement knowledge resulting from study of murine reproduction (Aplin and Ruane, 2017).

Our study also provides key knowledge regarding modeling pre-implantation development with cellular models. Embryonic signature comparison with pluripotent stem cells residing in various states of pluripotency showed that the established hierarchy of pluripotent stem cells mimics EPI: naive pluripotent cells are closest to pre-implantation EPI (5–8 dpf), whereas primed pluripotent cells, commonly used, are closer to post-implantation EPI (after 10 dpf) (Castel et al., 2020; Kilens et al., 2018; Liu et al., 2017; Takashima et al., 2014; Theunissen et al., 2014). We and others also discovered that naive pluripotent stem cells can convert to human trophoblast stem cells (hTSCs), which is reminiscent of late specification in human blastocysts (Castel et al., 2020; Cinkornpumin et al., 2020; Dong et al., 2020; Guo et al., 2021). Recently, we proposed that human trophoblast stem cells correspond to human day 8 post-implantation cytotrophoblast (Castel et al., 2020). Our study highlights the importance of knowledge about human peri-implantation development to understand pluripotent and trophoblast stem cell biology.

Our study clarifies the timing of molecular events and signaling pathways involved in human pre-implantation development. Fine-tuning those pathways will lead to more efficient medium formulation for embryo culture during IVF procedures. Improvement of IVF procedures is necessary because the procedural average efficiency is below 27% (European Society of Human Reproduction and Embryology, 2015). Ultimately, our study contributes to understanding human pre-implantation, a gateway to improve IVF success rates.

Limitations of study

A current limitation of human embryo work is the variability of human developmental time *in vitro*, which impairs the reproducibility of experiments. Our study provides a molecular blueprint of human development coupled to time-lapse staging. We unveiled numerous hypotheses and interactions that remain to be validated. Positional information could be improved to discriminate between polar TE and ICM. Fate specification needs to be addressed with lineage tracing approaches, and the importance of specific transcription factors will need to be assessed with CRISPR-Cas9 strategies, which remain restricted in most countries.

STAR★METHODS

Detailed methods are provided in the online version of this paper and include the following:

SUPPLEMENTAL INFORMATION

Supplemental information can be found online at https://doi.org/10.1016/j.stem.2021.04.027.

AUTHOR CONTRIBUTIONS

T.F. and L.D. designed the study. D.M., A. Bruneau, S.L., and L.D. wrote the manuscript with input from all authors. S.L., A.R., J.F., J.L., and A. Bruneau performed embryo manipulation. P.H., S.N., S.L., A. Bruneau, A.R., and L.D. performed IF analyses. A.R. and S.K. prepared scRNA-seq samples. M.S. and T.M. performed scRNA-seq. D.M., V.F.-C., and Y.L. performed bioinformatics analyses under the supervision of A. Bihouée and J.B. and with input from B.B. and G.C. T.F. and P.B. supervised human embryo donation. All authors approved the final version of the manuscript.

DECLARATION OF INTERESTS

The authors declare no competing interests.

INCLUSION AND DIVERSITY

We worked to ensure gender balance in the recruitment of human subjects. We worked to ensure that the study questionnaires were prepared in an inclusive way. One or more of the authors of this paper self-identifies as a member of the LGBTQ+ community. The author list of this paper includes contributors from the location where the research was conducted who participated in the data collection, design, analysis, and/or interpretation of the work.

REFERENCES

Aberkane, A., Essahib, W., Spits, C., De Paepe, C., Sermon, K., Adriaenssens, T., Mackens, S., Tournaye, H., Brosens, J.J., and Van de Velde, H. (2018). Expression of adhesion and extracellular matrix genes in human blastocysts upon attachment in a 2D co-culture system. Mol. Hum. Reprod. *24*, 375–387.

Acampora, D., Omodei, D., Petrosino, G., Garofalo, A., Savarese, M., Nigro, V., Di Giovannantonio, L.G., Mercadante, V., and Simeone, A. (2016). Loss of the Otx2-Binding Site in the Nanog Promoter Affects the Integrity of Embryonic Stem Cell Subtypes and Specification of Inner Cell Mass-Derived Epiblast. Cell Rep. *15*, 2651–2664.

Ahlström, A., Westin, C., Reismer, E., Wikland, M., and Hardarson, T. (2011). Trophectoderm morphology: an important parameter for predicting live birth after single blastocyst transfer. Hum. Reprod. *26*, 3289–3296.

Allègre, N., Chauveau, S., Dennis, C., Renaud, Y., Estrella, L.V., Pouchin, P., Cohen-Tannoudji, M., and Chazaud, C. (2019). A Nanog-dependent gene cluster initiates the specification of the pluripotent epiblast. bioRxiv. https://doi.org/10.1101/707679.

Alpha Scientists in Reproductive Medicine and ESHRE Special Interest Group of Embryology (2011). The Istanbul consensus workshop on embryo assessment: proceedings of an expert meeting. Hum. Reprod. *26*, 1270–1283.

Anders, S., Pyl, P.T., and Huber, W. (2015). HTSeq–a Python framework to work with high-throughput sequencing data. Bioinformatics *31*, 166–169.

Aplin, J.D., and Ruane, P.T. (2017). Embryo-epithelium interactions during implantation at a glance. J. Cell Sci. *130*, 15–22.

Apter, S., Ebner, T., Freour, T., Guns, Y., Kovacic, B., Le Clef, N., Marques, M., Meseguer, M., Montjean, D., Sfontouris, I., et al. (2020). Good practice recommendations for the use of time-lapse technology(dagger). Hum. Reprod. Open. *2020*, hoaa008.

Barcroft, L.C., Hay-Schmidt, A., Caveney, A., Gilfoyle, E., Overstrom, E.W., Hyttel, P., and Watson, A.J. (1998). Trophectoderm differentiation in the bovine embryo: characterization of a polarized epithelium. J. Reprod. Fertil. *114*, 327–339.

Barcroft, L.C., Offenberg, H., Thomsen, P., and Watson, A.J. (2003). Aquaporin proteins in murine trophectoderm mediate transepithelial water movements during cavitation. Dev. Biol. *256*, 342–354.

Bentin-Ley, U., Horn, T., Sjögren, A., Sorensen, S., Falck Larsen, J., and Hamberger, L. (2000). Ultrastructure of human blastocyst-endometrial interactions in vitro. J. Reprod. Fertil. *120*, 337–350.

Blakeley, P., Fogarty, N.M.E., del Valle, I., Wamaitha, S.E., Hu, T.X., Elder, K., Snell, P., Christie, L., Robson, P., and Niakan, K.K. (2015). Defining the three cell lineages of the human blastocyst by single-cell RNA-seq. Development *142*, 3151–3165.

Boroviak, T., Stirparo, G.G., Dietmann, S., Hernando-Herraez, I., Mohammed, H., Reik, W., Smith, A., Sasaki, E., Nichols, J., and Bertone, P. (2018). Single cell transcriptome analysis of human, marmoset and mouse embryos reveals common and divergent features of preimplantation development. Development *145*, dev167833.

Buecker, C., Srinivasan, R., Wu, Z., Calo, E., Acampora, D., Faial, T., Simeone, A., Tan, M., Swigut, T., and Wysocka, J. (2014). Reorganization of enhancer patterns in transition from naive to primed pluripotency. Cell Stem Cell *14*, 838–853.

Castel, G., Meistermann, D., Bretin, B., Firmin, J., Blin, J., Loubersac, S., Bruneau, A., Chevolleau, S., Kilens, S., Chariau, C., et al. (2020). Induction of Human Trophoblast Stem Cells from Somatic Cells and Pluripotent Stem Cells. Cell Rep. *33*, 108419.

Chan, C.J., Costanzo, M., Ruiz-Herrero, T., Mönke, G., Petrie, R.J., Bergert, M., Diz-Muñoz, A., Mahadevan, L., and Hiiragi, T. (2019). Hydraulic control of mammalian embryo size and cell fate. Nature *571*, 112–116.

Chazaud, C., and Yamanaka, Y. (2016). Lineage specification in the mouse preimplantation embryo. Development *143*, 1063–1074.

Chazaud, C., Yamanaka, Y., Pawson, T., and Rossant, J. (2006). Early lineage segregation between epiblast and primitive endoderm in mouse blastocysts through the Grb2-MAPK pathway. Dev. Cell *10*, 615–624.

Chen, X., Zhang, J., Wu, X., Cao, S., Zhou, L., Wang, Y., Chen, X., Lu, J., Zhao, C., Chen, M., and Ling, X. (2014). Trophectoderm morphology predicts outcomes of pregnancy in vitrified-warmed single-blastocyst transfer cycle in a Chinese population. J. Assist. Reprod. Genet. *31*, 1475–1481.

Cinkornpumin, J.K., Kwon, S.Y., Guo, Y., Hossain, I., Sirois, J., Russett, C.S., Tseng, H.W., Okae, H., Arima, T., Duchaine, T.F., et al. (2020). Naive Human Embryonic Stem Cells Can Give Rise to Cells with a Trophoblast-like Transcriptome and Methylome. Stem Cell Reports *15*, 198–213.

Ciray, H.N., Campbell, A., Agerholm, I.E., Aguilar, J., Chamayou, S., Esbert, M., and Sayed, S.; Time-Lapse User Group (2014). Proposed guidelines on the nomenclature and annotation of dynamic human embryo monitoring by a time-lapse user group. Hum. Reprod. *29*, 2650–2660.

De Mot, L., Gonze, D., Bessonnard, S., Chazaud, C., Goldbeter, A., and Dupont, G. (2016). Cell Fate Specification Based on Tristability in the Inner Cell Mass of Mouse Blastocysts. Biophys. J. *110*, 710–722.

De Paepe, C., Cauffman, G., Verloes, A., Sterckx, J., Devroey, P., Tournaye, H., Liebaers, I., and Van de Velde, H. (2013). Human trophectoderm cells are not yet committed. Hum. Reprod. *28*, 740–749.

De Paepe, C., Aberkane, A., Dewandre, D., Essahib, W., Sermon, K., Geens, M., Verheyen, G., Tournaye, H., and Van de Velde, H. (2019). BMP4 plays a role in apoptosis during human preimplantation development. Mol. Reprod. Dev. *86*, 53–62.

Deglincerti, A., Croft, G.F., Pietila, L.N., Zernicka-Goetz, M., Siggia, E.D., and Brivanlou, A.H. (2016). Self-organization of the in vitro attached human embryo. Nature *533*, 251–254.

Dong, C., Beltcheva, M., Gontarz, P., Zhang, B., Popli, P., Fischer, L.A., Khan, S.A., Park, K.M., Yoon, E.J., Xing, X., et al. (2020). Derivation of trophoblast stem cells from naïve human pluripotent stem cells. eLife *9*, e52504.

Dumortier, J.G., Le Verge-Serandour, M., Tortorelli, A.F., Mielke, A., de Plater, L., Turlier, H., and Maître, J.L. (2019). Hydraulic fracturing and active coarsening position the lumen of the mouse blastocyst. Science *365*, 465–468.

Ester, M., Kriegel, H.P., Sander, J., and Xu, X. (1996). A density-based algorithm for discovering clusters in large spatial databases with noise. In Proceedings of the Second International Conference on Knowledge Discovery and Data Mining, pp. 226–231.

European Society of Human Reproduction and Embryology (2015). Data collection and research. https://www.eshre.eu/.

Feyeux, M., Reignier, A., Mocaer, M., Lammers, J., Meistermann, D., Barrière, P., Paul-Gilloteaux, P., David, L., and Fréour, T. (2020). Development of automated annotation software for human embryo morphokinetics. Hum. Reprod. *35*, 557–564.

Fogarty, N.M.E., McCarthy, A., Snijders, K.E., Powell, B.E., Kubikova, N., Blakeley, P., Lea, R., Elder, K., Wamaitha, S.E., Kim, D., et al. (2017). Genome editing reveals a role for OCT4 in human embryogenesis. Nature *550*, 67–73.

Frum, T., Murphy, T.M., and Ralston, A. (2018). HIPPO signaling resolves embryonic cell fate conflicts during establishment of pluripotency in vivo. eLife *7*, e42298.

Gardner, D.K., Lane, M., Stevens, J., Schlenker, T., and Schoolcraft, W.B. (2000). Blastocyst score affects implantation and pregnancy outcome: towards a single blastocyst transfer. Fertil. Steril. *73*, 1155–1158.

Gerri, C., McCarthy, A., Alanis-Lobato, G., Demtschenko, A., Bruneau, A., Loubersac, S., Fogarty, N.M.E., Hampshire, D., Elder, K., Snell, P., et al. (2020). Initiation of a conserved trophectoderm program in human, cow and mouse embryos. Nature *587*, 443–447.

Giacomini, G., Tabizadeh, S.S., Satyaswaroop, P.G., Bonsi, L., Vitale, L., Bagnara, G.P., Strippoli, P., and Jasonni, V.M. (1995). Epithelial cells are the major source of biologically active granulocyte macrophage colony-stimulating factor in human endometrium. Hum. Reprod. *10*, 3259–3263.

Giocanti-Auregan, A., Vacca, O., Bénard, R., Cao, S., Siqueiros, L., Montañez, C., Paques, M., Sahel, J.A., Sennlaub, F., Guillonneau, X., et al. (2016). Altered astrocyte morphology and vascular development in dystrophin-Dp71-null mice. Glia *64*, 716–729.

Grabarek, J.B., Zyzyńska, K., Saiz, N., Piliszek, A., Frankenberg, S., Nichols, J., Hadjantonakis, A.K., and Plusa, B. (2012). Differential plasticity of epiblast and primitive endoderm precursors within the ICM of the early mouse embryo. Development *139*, 129–139.

Graham, S.J., and Zernicka-Goetz, M. (2016). The Acquisition of Cell Fate in Mouse Development: How Do Cells First Become Heterogeneous? Curr. Top. Dev. Biol. *117*, 671–695.

Greenberg, M.V.C., and Bourc'his, D. (2019). The diverse roles of DNA methylation in mammalian development and disease. Nat. Rev. Mol. Cell Biol. *20*, 590–607.

Grewal, S., Carver, J.G., Ridley, A.J., and Mardon, H.J. (2008). Implantation of the human embryo requires Rac1-dependent endometrial stromal cell migration. Proc. Natl. Acad. Sci. USA *105*, 16189–16194.

Gu, Z., Eils, R., and Schlesner, M. (2016). Complex heatmaps reveal patterns and correlations in multidimensional genomic data. Bioinformatics *32*, 2847–2849.

Guo, G., Stirparo, G.G., Strawbridge, S.E., Spindlow, D., Yang, J., Clarke, J., Dattani, A., Yanagida, A., Li, M.A., Myers, S., et al. (2021). Human naive epiblast cells possess unrestricted lineage potential. Cell Stem Cell.

Guzman-Ayala, M., Ben-Haim, N., Beck, S., and Constam, D.B. (2004). Nodal protein processing and fibroblast growth factor 4 synergize to maintain a trophoblast stem cell microenvironment. Proc. Natl. Acad. Sci. USA *101*, 15656–15660.

Handyside, A.H. (1978). Time of commitment of inside cells isolated from pre-implantation mouse embryos. J. Embryol. Exp. Morphol. *45*, 37–53.

Hannan, N.J., Paiva, P., Dimitriadis, E., and Salamonsen, L.A. (2010). Models for study of human embryo implantation: choice of cell lines? Biol. Reprod. *82*, 235–245.

Hill, M.J., Richter, K.S., Heitmann, R.J., Graham, J.R., Tucker, M.J., DeCherney, A.H., Browne, P.E., and Levens, E.D. (2013). Trophectoderm grade predicts outcomes of single-blastocyst transfers. Fertil. Steril. *99*, 1283–1289.e1.

Hirate, Y., Hirahara, S., Inoue, K., Suzuki, A., Alarcon, V.B., Akimoto, K., Hirai, T., Hara, T., Adachi, M., Chida, K., et al. (2013). Polarity-dependent distribution of angiomotin localizes Hippo signaling in preimplantation embryos. Curr. Biol. *23*, 1181–1194.

Jedrusik, A., Parfitt, D.E., Guo, G., Skamagki, M., Grabarek, J.B., Johnson, M.H., Robson, P., and Zernicka-Goetz, M. (2008). Role of Cdx2 and cell polarity in cell allocation and specification of trophectoderm and inner cell mass in the mouse embryo. Genes Dev. *22*, 2692–2706.

Kilens, S., Meistermann, D., Moreno, D., Chariau, C., Gaignerie, A., Reignier, A., Lelièvre, Y., Casanova, M., Vallot, C., Nedellec, S., et al.; Milieu Intérieur Consortium (2018). Parallel derivation of isogenic human primed and naive induced pluripotent stem cells. Nat. Commun. *9*, 360.

Kimmelman, J., Heslop, H.E., Sugarman, J., Studer, L., Benvenisty, N., Caulfield, T., Hyun, I., Murry, C.E., Sipp, D., and Daley, G.Q. (2016). New ISSCR guidelines: clinical translation of stem cell research. Lancet *387*, 1979–1981.

Korotkevich, G., Sukhov, V., and Sergushichev, A. (2019). Fast gene set enrichment analysis. bioRxiv. https://doi.org/10.1101/060012.

Kuijk, E.W., van Tol, L.T., Van de Velde, H., Wubbolts, R., Welling, M., Geijsen, N., and Roelen, B.A. (2012). The roles of FGF and MAP kinase signaling in the segregation of the epiblast and hypoblast cell lineages in bovine and human embryos. Development *139*, 871–882.

La Manno, G., Soldatov, R., Zeisel, A., Braun, E., Hochgerner, H., Petukhov, V., Lidschreiber, K., Kastriti, M.E., Lönnerberg, P., Furlan, A., et al. (2018). RNA velocity of single cells. Nature *560*, 494–498.

Langfelder, P., and Horvath, S. (2008). WGCNA: an R package for weighted correlation network analysis. BMC Bioinformatics *9*, 559.

Lindenberg, S. (1991). Experimental studies on the initial trophoblast endometrial interaction. Dan. Med. Bull. 38, 371–380.

Liu, Z.P., Wu, C., Miao, H., and Wu, H. (2015). RegNetwork: an integrated database of transcriptional and post-transcriptional regulatory networks in human and mouse. Database 2015, bav095.

Liu, X., Nefzger, C.M., Rossello, F.J., Chen, J., Knaupp, A.S., Firas, J., Ford, E., Pflueger, J., Paynter, J.M., Chy, H.S., et al. (2017). Comprehensive characterization of distinct states of human naive pluripotency generated by reprogramming. Nat. Methods 14, 1055–1062.

Lun, A.T., McCarthy, D.J., and Marioni, J.C. (2016). A step-by-step workflow for low-level analysis of single-cell RNA-seq data with Bioconductor. F1000Res. 5, 2122.

McInnes, L., Healy, J., and Melville, J. (2018). UMAP: Uniform Manifold Approximation and Projection for Dimension Reduction. arXiv, 1802.03426, arXiv. https://arxiv.org/abs/1802.03426.

Niakan, K.K., and Eggan, K. (2013). Analysis of human embryos from zygote to blastocyst reveals distinct gene expression patterns relative to the mouse. Dev. Biol. 375, 54–64.

Petropoulos, S., Edsgärd, D., Reinius, B., Deng, Q., Panula, S.P., Codeluppi, S., Plaza Reyes, A., Linnarsson, S., Sandberg, R., and Lanner, F. (2016). Single-Cell RNA-Seq Reveals Lineage and X Chromosome Dynamics in Human Preimplantation Embryos. Cell 165, 1012–1026.

Posfai, E., Petropoulos, S., de Barros, F.R.O., Schell, J.P., Jurisica, I., Sandberg, R., Lanner, F., and Rossant, J. (2017). Position- and Hippo signaling-dependent plasticity during lineage segregation in the early mouse embryo. eLife 6, e22906.

Qiu, X., Mao, Q., Tang, Y., Wang, L., Chawla, R., Pliner, H.A., and Trapnell, C. (2017). Reversed graph embedding resolves complex single-cell trajectories. Nat. Methods 14, 979–982.

Ramos-Ibeas, P., Sang, F., Zhu, Q., Tang, W.W.C., Withey, S., Klisch, D., Wood, L., Loose, M., Surani, M.A., and Alberio, R. (2019). Pluripotency and X chromosome dynamics revealed in pig pre-gastrulating embryos by single cell analysis. Nat. Commun. 10, 500.

Reijo Pera, R.A., and Prezzoto, L. (2016). Species-Specific Variation Among Mammals. Curr. Top. Dev. Biol. 120, 401–420.

Rivron, N.C., Frias-Aldeguer, J., Vrij, E.J., Boisset, J.C., Korving, J., Vivié, J., Truckenmüller, R.K., van Oudenaarden, A., van Blitterswijk, C.A., and Geijsen, N. (2018). Blastocyst-like structures generated solely from stem cells. Nature 557, 106–111.

Roode, M., Blair, K., Snell, P., Elder, K., Marchant, S., Smith, A., and Nichols, J. (2012). Human hypoblast formation is not dependent on FGF signalling. Dev. Biol. 361, 358–363.

Rossant, J., and Lis, W.T. (1979). Potential of isolated mouse inner cell masses to form trophectoderm derivatives in vivo. Dev. Biol. 70, 255–261.

Roy, A., Ghosh, A., Kumar, B., and Chandran, B. (2019). IFI16, a nuclear innate immune DNA sensor, mediates epigenetic silencing of herpesvirus genomes by its association with H3K9 methyltransferases SUV39H1 and GLP. eLife 8, e49500.

Sergushichev, A.A. (2016). An algorithm for fast preranked gene set enrichment analysis using cumulative statistic calculation. bioRxiv. https://doi.org/10.1101/060012.

Shahbazi, M.N., Jedrusik, A., Vuoristo, S., Recher, G., Hupalowska, A., Bolton, V., Fogarty, N.N.M., Campbell, A., Devito, L., Ilic, D., et al. (2016). Self-organization of the human embryo in the absence of maternal tissues. Nat. Cell Biol. 18, 700–708.

Shahbazi, M.N., Scialdone, A., Skorupska, N., Weberling, A., Recher, G., Zhu, M., Jedrusik, A., Devito, L.G., Noli, L., Macaulay, I.C., et al. (2017). Pluripotent state transitions coordinate morphogenesis in mouse and human embryos. Nature 552, 239–243.

Shoukir, Y., Chardonnens, D., Campana, A., Bischof, P., and Sakkas, D. (1998). The rate of development and time of transfer play different roles in influencing the viability of human blastocysts. Hum. Reprod. 13, 676–681.

Singh, M., Widmann, T.J., Bansal, V., Cortes, J.L., Schumann, G.G., Wunderlich, S., Martin, U., Garcia-Canadas, M., Garcia-Perez, J.L., Hurst, L.D., and Izsvak, Z. (2019). The selection arena in early human blastocysts resolves the pluripotent inner cell mass. BioRxiv 318329.

Stirparo, G.G., Boroviak, T., Guo, G., Nichols, J., Smith, A., and Bertone, P. (2018). Integrated analysis of single-cell embryo data yields a unified transcriptome signature for the human pre-implantation epiblast. Development 145, dev158501.

Takashima, Y., Guo, G., Loos, R., Nichols, J., Ficz, G., Krueger, F., Oxley, D., Santos, F., Clarke, J., Mansfield, W., et al. (2014). Resetting transcription factor control circuitry toward ground-state pluripotency in human. Cell 158, 1254–1269.

Theunissen, T.W., Powell, B.E., Wang, H., Mitalipova, M., Faddah, D.A., Reddy, J., Fan, Z.P., Maetzel, D., Ganz, K., Shi, L., et al. (2014). Systematic identification of culture conditions for induction and maintenance of naive human pluripotency. Cell Stem Cell 15, 471–487.

Theunissen, T.W., Friedli, M., He, Y., Planet, E., O'Neil, R.C., Markoulaki, S., Pontis, J., Wang, H., Iouranova, A., Imbeault, M., et al. (2016). Molecular Criteria for Defining the Naive Human Pluripotent State. Cell Stem Cell 19, 502–515.

Thompson, S.M., Onwubalili, N., Brown, K., Jindal, S.K., and McGovern, P.G. (2013). Blastocyst expansion score and trophectoderm morphology strongly predict successful clinical pregnancy and live birth following elective single embryo blastocyst transfer (eSET): a national study. J. Assist. Reprod. Genet. 30, 1577–1581.

Tiegs, A.W., Sun, L., Patounakis, G., and Scott, R.T. (2019). Worth the wait? Day 7 blastocysts have lower euploidy rates but similar sustained implantation rates as Day 5 and Day 6 blastocysts. Hum. Reprod. 34, 1632–1639.

Trombetta, J.J., Gennert, D., Lu, D., Satija, R., Shalek, A.K., and Regev, A. (2014). Preparation of Single-Cell RNA-Seq Libraries for Next Generation Sequencing. Curr. Protoc. Mol. Biol. 107, 4.22.1-17.

White, M.D., Zenker, J., Bissiere, S., and Plachta, N. (2018). Instructions for Assembling the Early Mammalian Embryo. Dev. Cell 45, 667–679.

Xiang, L., Yin, Y., Zheng, Y., Ma, Y., Li, Y., Zhao, Z., Guo, J., Ai, Z., Niu, Y., Duan, K., et al. (2020). A developmental landscape of 3D-cultured human pre-gastrulation embryos. Nature 577, 537–542.

Xiong, Y., Tan, Y.J., Xiong, Y.M., Huang, Y.T., Hu, X.L., Lu, Y.C., Ye, Y.H., Wang, T.T., Zhang, D., Jin, F., et al. (2013). Expression of aquaporins in human embryos and potential role of AQP3 and AQP7 in preimplantation mouse embryo development. Cell. Physiol. Biochem. 31, 649–658.

Yamagata, T., and Yamazaki, K. (1991). Implanting mouse embryo stain with a LNF-I bearing fluorescent probe at their mural trophectodermal side. Biochem. Biophys. Res. Commun. 181, 1004–1009.

Yan, L., Yang, M., Guo, H., Yang, L., Wu, J., Li, R., Liu, P., Lian, Y., Zheng, X., Yan, J., et al. (2013). Single-cell RNA-Seq profiling of human preimplantation embryos and embryonic stem cells. Nat. Struct. Mol. Biol. 20, 1131–1139.

Zhou, F., Wang, R., Yuan, P., Ren, Y., Mao, Y., Li, R., Lian, Y., Li, J., Wen, L., Yan, L., et al. (2019). Reconstituting the transcriptome and DNA methylome landscapes of human implantation. Nature 572, 660–664.

Ziebe, S., Loft, A., Povlsen, B.B., Erb, K., Agerholm, I., Aasted, M., Gabrielsen, A., Hnida, C., Zobel, D.P., Munding, B., et al. (2013). A randomized clinical trial to evaluate the effect of granulocyte-macrophage colony-stimulating factor (GM-CSF) in embryo culture medium for in vitro fertilization. Fertil. Steril. 99, 1600–1609.

STAR★METHODS

KEY RESOURCES TABLE

REAGENT or RESOURCE	SOURCE	IDENTIFIER
Antibodies		
IFI16	Novusbio	Cat# NBP1-83118; RRID:AB_11041205
AQP3	Antibodies-online	Cat# ABIN863208
NR2F2	Abcam	Cat# ab211776
GATA2	Sigma	Cat# WH0002624M1; RRID:AB_1841726
CDH1	Abcam	Cat# ab1416; RRID:AB_300946
GATA3	R&D systems	Cat# AF2605; RRID:AB_2108571
NANOG	R&D systems	Cat# AF1997; RRID:AB_355097
SOX17	R&D systems	Cat# AF1924; RRID:AB_355060
ZO1	Invitrogen	Cat# 40-2200; RRID:AB_2533456
NANOG	Thermofisher	Cat# PA1-097; RRID:AB_2539867
GATA4	Invitrogen	Cat# 14-9980-82; RRID:AB_763541
IFI16	Abcam	Cat# ab55328; RRID:AB_943797
OTX2	R&D	Cat# AF1979; RRID:AB_2157172
Donkey anti rabbit Alexa Fluor 488	Life Technologies	Cat#A21206; RRID:AB_2535792
Donkey anti mouse Alexa Fluor 488	Life Technologies	Cat#A21202; RRID:AB_141607
Donkey anti rabbit Alexa Fluor 568	Life Technologies	Cat#A10042; RRID:AB_2534017
Donkey anti mouse Alexa Fluor 568	Life Technologies	Cat#A10037; RRID:AB_2534013
Donkey anti goat Alexa Fluor 568	Life Technologies	Cat#A11057; RRID:AB_2534104
Donkey anti goat Alexa Fluor 647	Life Technologies	Cat#A21447; RRID:AB_2535864
Donkey anti rat DyLight 550	Thermofisher	Cat#SA5-10027; RRID:AB_2556607
Donkey anti mouse Alexa Fluor Plus 647	Life Technologies	Cat#A32787; RRID:AB_2762830
Biological samples		
Human pre-implantation embryos from 8 cells to B5 stage	Assisted Reproductive Technology unit of the University Hospital of Nantes	Authorized project: RE13-010 and RE18-010
Chemicals, peptides, and recombinant proteins		
RapidWarmBlast	Vitrolife	10120
RapidWarCleave	Vitrolife	10118
G2 plus	Vitrolife	10132
HSA solution	Vitrolife	10064
G-PGD	Vitrolife	10074
GTL	Vitrolife	10145
IVC1 medium	Cell guidance systems	M11-6
IVC2 medium	Cell guidance systems	M12-6
Deposited data		
scRNA-seq original data	This paper; ENA	https://www.ebi.ac.uk/ena/browser/view/PRJEB30442
scRNA-Seq alignment pipeline	This paper; GitLab	https://gitlab.univ-nantes.fr/E114424Z/SingleCell_Align
scRNA-Seq preprocessing and normalization	This paper; GitLab	https://gitlab.univ-nantes.fr/E114424Z/singlecellnormalize
WGCNA workflow	This paper; GitLab	https://gitlab.univ-nantes.fr/E114424Z/WGCNA
Monocle2 workflow, UMAP and cell clustering	This paper; GitLab	https://gitlab.univ-nantes.fr/E114424Z/monocle2_workflow

(Continued on next page)

Continued

REAGENT or RESOURCE	SOURCE	IDENTIFIER
Pseudotime User Interface source code	This paper; GitLab	https://gitlab.univ-nantes.fr/E114424Z/ptuihost
Software and algorithms		
Volocity	Quorum technologies	V6.3
Fiji	ImageJ	V1.53c
R	Bioconductor	v 4.0.3

RESOURCE AVAILABILITY

Lead contact
Further information and requests should be directed to the Lead Contact, Laurent DAVID (laurent.david@univ-nantes.fr)

Materials availability
This study did not generate new unique reageants

Data and code availability
The accession number for the original scRNA-seq data reported in this paper is ENA: PRJEB30442.
 The source code can be retrieved by following the links below.
 scRNaseq alignment pipeline:

 https://gitlab.univ-nantes.fr/E114424Z/SingleCell_Align

 scRNaseq preprocessing and normalization:

 https://gitlab.univ-nantes.fr/E114424Z/singlecellnormalize

 WGCNA workflow:

 https://gitlab.univ-nantes.fr/E114424Z/WGCNA

 Monocle2 workflow, UMAP and cell clustering:

 https://gitlab.univ-nantes.fr/E114424Z/monocle2_workflow

 Pseudotime User Interface source code:

 https://gitlab.univ-nantes.fr/E114424Z/ptuihost

 All other parts of the code are available upon request

EXPERIMENTAL MODEL AND SUBJECT DETAILS

Human pre-implantation embryos
The use of human embryo donated to research as surplus of IVF treatment was allowed by the French embryo research oversight committee: Agence de la Biomédecine, under approval number RE13-010 and RE18-010. All human pre-implantation embryos used in this study were obtained from and cultured at the Assisted Reproductive Technology unit of the University Hospital of Nantes, France, which are authorized to collect embryos for research under approval number AG110126AMP of the Agence de la Bio-médecine. Embryos used were initially created in the context of an assisted reproductive cycle with a clear reproductive aim and then voluntarily donated for research once the patients have fulfilled their reproductive needs or tested positive for the presence of monogenic diseases. Informed written consent was obtained from both parents of all couples that donated spare embryos following IVF treatment. Before giving consent, people donating embryos were provided with all of the necessary information about the research project and opportunity to receive counselling. No financial inducements are offered for donation. Molecular analysis of the embryos was performed in compliance with the embryo research oversight committee and The International Society for Stem Cell Research (ISSCR) guidelines (Kimmelman et al., 2016).

METHOD DETAILS

Human pre-implantation embryos culture
Human embryos were thawed following the manufacturer's instructions (Cook Medical: Sydney IVF Thawing kit for slow freezing and Vitrolife: RapidWarmCleave or RapidWarmBlast for vitrification). Human embryos frozen at 8-cell stage were loaded in a 12-well dish

(Vitrolife: Embryoslide Ibidi) with non-sequential culture media (Vitrolife G2 plus) under mineral oil (Origio: Liquid Paraffin), at 37°C, in 5% O_2/6% CO_2.

Human embryo prolonged culture

Embryos cultured for 5 days (11xB3 and 5xB4 blastocysts) were thawed as described above. The *zona pellucida* (ZP) of each embryo was removed by brief laser impulse followed by manual extrusion or aspiration of the embryo. Zona pellucida free embryos were washed in GTL medium and immediately transferred in 8-well IbiTreat μ-plates (IB-80826; Ibidi GmbH) with 300μL IVC1 medium (M11-6, Cell Guidance systems) (Deglincerti et al., 2016) and cultured at 37°C, in 21% O2/5% CO2. After 48h of *in vitro* culture (day 2), 250μL of IVC1 was replaced with 250μL of IVC2 medium (M12-6, Cell Guidance systems). At B3 or B4 + 72h *in vitro* culture, 11/16 embryos (69%) were attached, 3 (19%) were floating and 2 (12%) disagregated.

Human embryo time-lapse imaging

Embryos were loaded into the Embryoscope® (Vitrolife®), a tri-gas incubator with a built-in microscope allowing time-lapse monitoring of embryo development. Images were captured on seven focal plans every 15-min intervals using Hoffman modulation contrast (HMC) optical setup[1] and a 635 nm LED as light source as provided in the Embryoscope®. The resolution of the camera is 1280x1024 pixels. The development of each embryo was prospectively annotated as described by Ciray et al., by two trained embryologists undergoing regular internal quality control in order to keep inter-operator variability as low as possible (Ciray et al., 2014). ZP thickness was measured by our analysis pipeline (Feyeux et al., 2020). The term tM refers to a fully compacted morula. At the blastocyst stage, tSB is used to describe the onset of a cavity formation, tB is used for full blastocyst i.e the last frame before the ZP starts to thin, tEB for expanded blastocyst, i.e., when the ZP is 50% thinned. Blastocyst contractions and the beginning of herniation were also recorded.

Immunofluorescence of human embryos

Embryos were fixed at the morula, B1, B2, B3, B4, B5 or B6 stages according to the grading system proposed by Gardner and Schoolcraft (Gardner et al., 2000) or at B3 or B4 + 72h *in vitro* culture. Embryos were fixed with 4% paraformaldehyde for 5 min at room temperature and washed in PBS/BSA. Embryos were permeabilized and blocked in IF Buffer (PBS–0.2% Triton, 10% FBS) at room temperature for 60 min. Samples were incubated with primary antibodies over-night at 4°C. Incubation with secondary antibodies was performed for 2 hours at room temperature along with DAPI counterstaining. Primary and secondary antibodies with dilutions used in this study are listed in Table S4.

Imaging

Confocal immunofluorescence pictures were taken with a Nikon confocal microscope and a 20 × Mim objective. Optical sections of 1μm-thick were collected. The images were processed using Fiji (https://fiji.sc/) and Volocity 6.3 visualization softwares. Volocity software was used to detect and count nuclei. Two experienced operators graded nuclei signal for each IF channel. Grading was perform independently and counts were then averaged. A nucleus is considered positive for staining if signal is clearly higher than background. "High" or "low" positive staining is up to each operator according to the general signal intensity for each channel. Several embryos were photobleached in order to restain it (Figure 6C; Figures S6A and S6B). Under Nikon A1 confocal, lasers at 568nm and 647nm were set to 100% power for 10min. The NR2F2 (Rabbit / 488) – SOX17 (Goat / 647) – IFI16 (Mouse / 568) stained embryos were restained with NR2F2 (Rabbit / 488) – GATA4 (Rat / 568) – IFI16 (Mouse / 647). Scale of Figure S1E was estimated with the diameter of the STRIPPER® tip.

Single-cell isolation

PGD-trained people performed brief laser impulses to separate the polar TE and ICM and mural TE of blastocysts. Embryos were then incubated 10min in G-PGD/HSA (Vitrolife®) and transferred in accutase. Embryos were triturated with gentle pipette flush under binocular magnifier for 3-4min. Single-cells/clumps were washed in GTL (Vitrolife®) and triturated again if necessary. Single-cells were picked one by one with IVF-lab capillaries.

QUANTIFICATION AND STATISTICAL ANALYSIS

Single-cell RNA sequencing

Single-cell isolation and overall dataset are presented in Figure S1 and Tables S1 and S5. Single-cell RNA-seq libraries were prepared according to the SmartSeq2 protocol with some modifications (Trombetta et al., 2014). Briefly, total RNA was purified using RNA-SPRI beads. Poly(A)[+] mRNA was reverse-transcribed to cDNA which was then amplified. cDNA was subject to transposon-based fragmentation that used dual-indexing to barcode each fragment of each converted transcript with a combination of barcodes specific to each sample. In the case of single cell sequencing, each cell was given its own combination of barcodes. Barcoded cDNA fragments were then pooled prior to sequencing. Sequencing was carried out as paired end 2x25bp with an additional 8 cycles for each index. The FASTQ files were mapped with Hisat2 on GRChH38 genome version, downloaded from ensembl.org. HTSeq (Anders et al., 2015) was used to generate raw counts tables from BAM files, using the matching GTF for the reference genome.

Raw count table treatments
Samples were filtered with the use of the R function *isOutlier* from SCRAN (Lun et al., 2016) library. This function tags samples as outliers with a threshold based on median derivation away from the median of the metric. We filtered samples with two metrics: the number of expressed genes with a threshold of 2 median away derivation from median, and the total number of counts in the sample with a threshold of 3 median away derivation from median. Both metrics were used to discard samples in a two-sided way, below and above the median. This two-sided filter was applied to remove samples carrying too little (93876 counts - 5558 genes) or too much (80431229 counts – 18711 genes) information. Indeed, these are considered as potential doublet events. Genes that were expressed in less than two cells and with an average expression less than 0.1 were removed.

The four datasets were then normalized together using the *computeSumFactor* function from SCRAN. Logged and non-logged data were collected using the *normalize* function from scater R library. To compute batch effect free expression, we normalized the data as described above but per dataset. We used mutual nearest neighbors correction implemented by the function *mnnCorrect* to achieve the batch correction from the log-normalized data. The reference dataset that were used for *mnnCorrect* is from Petropoulos et al. (2016).

Computation of pseudotime
Monocle2 needs a subset of genes to make the dimensionality reduction and pseudotimes trajectories. To choose the best set of ordering genes we took samples that passed the quality control from Petropoulos et al. (2016) to avoid batch effects. We used SCRAN for processing size factors (normalization factor). We then created an R object with the *newCellDataSet* object used by Monocle2 with the raw expression and the expressionFamily parameter set as "negbinomial.size()." Size factors were attributed according to the SCRAN results. The next step consisted of estimating empirical dispersion of each gene in the negative binomial model with the *estimateDispersions* function. We used the dispersion table function to gather the empirical dispersion and the fitted theoretical dispersion for each gene. We made a ratio of empirical dispersion on the theoretical dispersion for each gene. This ratio describes an over-dispersion score.

For a given gene *i* the over-dispersion score S is calculated as follows: $S_i = \frac{\sigma^2_{emp\ i}}{\sigma^2_{theo\ \mu_i}}$

Genes with an average log expression < 0.5 across samples were filtered out. Remaining genes were ranked based on their over-dispersion score.

Pseudotimes were generated using a range of top ranked ordering genes from the top 500 to the top 5500. This led to 5000 pseudotimes. For each pseudotime, A new R object was created with the newCellDataSet function, with the batch corrected expression from the four datasets as input and the expressionFamily parameter set as "gaussianff()." Selected ordering genes were then set as input of Monocle2 algorithm, with the number of resulting dimensions set to three dimensions. An automatic classification of pseudotimes was set up following three criteria based on their topology:

- Number of branches populated by mural TE cells.
- Succession of developmental stage.
- Position and number of branching points.

The most common topologies were: (i) all mural TE cells within one branch, (ii) developmental stages succeeding one other, i.e., morula between 8-cell and blastocysts, (iii) two branching points, (iv) first branching point at E5. The chosen pseudotime belonged systematically to the most abundant topologies and is calculated from 4484 ordering genes. The resulting 3-dimension pseudotime was rotated to obtain a 2-dimensional projection.

WGCNA
WGCNA (Langfelder and Horvath, 2008) was performed on batch corrected data using a soft power of 10 with signed Pearson correlation. Resulting module were manually curated to choose a set of 8 modules that were well represented in data and that have distinct behaviors. For each module we use the module eigengene metric that is given by WGCNA to infer the global module expression across the samples. A loess regression of eigengene by pseudotime was used for Figure S4C. Gene list for each module can be found in Table S3.

UMAP and cell clustering
UMAP was computed with the R library uwot. Module eigengenes from the 8 studied WGCNA modules were used as features for the UMAP algorithm. The n_neighbors parameter was set to 1751 (size of the dataset) and min_dist = 0.01. Density clustering of cells was performed with dbscan with eps = 0.21 and minPts = 5. 52 outliers were attributed manually to existing clusters. An additional kmeans (k = 2) was performed on the main TE cluster from NR2F2 and GATA2 module eigengenes to separate the medium and the late TE (Korotkevich et al., 2019; Sergushichev, 2016).

Loess regressed expression by pseudotime
We used a Locally Weighted Regression (LOESS) to fit expression in the pseudotime by cell fate with a neighbor impact of 0.75. Expression profiles of common segments were fitted to extract global tendencies. A last LOESS was computed with a low neighbor impact to merge segments to obtain continuous expression curves.

Subdivision of pseudotime branches

The original pseudotime was constituted by five states, as Monocle2 separates states only by branching point. We subdivided pre-specification and trophectoderm branch samples by using WGCNA module eigengene. For both branches, WGCNA modules with a Pearson correlation higher than 0.75 with the pseudotime were selected. A loess regression of these module eigengene by pseudotime was performed, followed by a hierarchical clustering of regressed module eigengenes. The clustering was then partitioned. For each branch the best partition was determined at three clusters with the greatest relative loss of inertia method.

Data representation used in each figure

Raw expression:

- estimation of gene dispersion and select ordering genes

Normalized expression:

- projection of gene expression on pseudotime or UMAP (Figures 1C and 1E; Figure S3B)
- Heatmap (Figure 2C)
- Pseudotime User Interface (Figure S4E)

Loess regressed expression by pseudotime:

- expression profile curves (Figure S7)

Batch corrected logged expression:

- computation of pseudotime
- computation of WGCNA modules

ComplexHeatmap (Gu et al., 2016), ggplot2 and d3.js. were used for graphical representation. Hierarchical clustering was done using the Ward criteria and from a correlation distance for the gene/pathway eigengenes, or from the euclidean distance for other metrics.

Mouse single-cell RNA-Seq analysis

Mouse dataset were analyzed in a similar way to human datasets, without batch correction. Alignment step was done from the mm10 version of the genome. Timing of blastulation is corroborated by time-lapse. Cell annotations can be found in Table S2.

RNA velocity

RNA velocity was performed from BAM of samples that have passed all quality control in the final counts table. First, we used velocyto.py using the command *velocyto run*, with the parameter–logic as "SmartSeq2," and the parameter -m (RepeatMasker annotations) as a GTF downloaded from the UCSC genome browser. The global GTF was the same that were used for the computation of raw counts table. Resulting loom files were merged using loompy.combine from lompy python package. We used velocyto.R for computing Velocity matrix. Loom files were read with the function *read.loom.matrices*. Then we separated spliced reads matrix, unspliced reads matrix and spanning reads matrix. For each of the matrices gene filtering was performed with the function *filter.genes.by.cluster.expression*. The min.max.cluster.average parameters were set for the corresponding matrix as:

- spliced reads matrix: 5
- unspliced reads matrix: 1
- spanning reads matrix: 0.5

Then RNA velocity was estimated using *gene.relative.velocity.estimates*, with the following parameters: fit.quantile = 0.05, deltaT = 1, kCells = 5.

PCA of Figures 3D and 3E were calculated with the function *pca.velocity.plot*.

RNA velocity vectors were projected on an isometric representation of the UMAP (Figures 3F, 3G, 5G, and 5H) with the function *show.velocity.on.embedding.cor*. Only the cells from the Petrolopoulos et al. dataset are projected to avoid batch effects during the computation of RNA velocities.

In the Figures 3F and 3G, the limit between the sector of early TE and EPI is the bisector of the angle formed by the cluster centroid of EPI, B1 & B2 and early TE in the UMAP.

In the Figures 5G and 5H, the sector of the circular diagram was oriented to face the centroid of the PrE cluster from the centroid of the EPI.PrE cluster.

Enrichment analysis

Module enrichment analysis was performed with FGSEA (Sergushichev, 2016). Ranking metric for f GSEA was set as WGCNA gene module membership (Korotkevich et al., 2019). This score is processed by Pearson correlation of module eigengene and gene expression. Enrichment was made on five databases: Gene ontology (Cellular Component, Molecular Function and Biological Process), Reactom and KEGG. All retained term were enriched below an adjusted Benjamini-Hochberg p value of 0.05. A list of transcriptional factors (TF) was downloaded from the RegNetwork database (Liu et al., 2015). Pathway eigengene metric (Figure S4D) was processed by taking the first component of a principal component analysis of genes from each enriched term.